water

MDPI

Article

Mechanisms of Thick-Hard Roof and Thin Aquifer Zone Floor Destruction and the Evolution Law of Water Inrush

Min Cao [1,*], Shangxian Yin [1,*], Shuqian Li [2] and Xu Wang [1]

[1] Hebei State Key Laboratory of Mine Disaster Prevention, North China Institute of Science and Technology, Beijing 101601, China; jgqsqq0106@163.com
[2] School of Earth Sciences and Surveying Engineering, China University of Mining and Technology, Beijing 100083, China; lsq_cumtb@163.com
* Correspondence: caomin727@163.com (M.C.); yinshx03@126.com (S.Y.)

Abstract: The collapse of thick-hard roofs after coal has been extracted is not a consequential process in all cases. Rather, it happens due to the augmentation of high stress conducted at depth, followed by a wider range of damage as the floor cracks. The extent and spread of the cracks in the floor indicate the intensity of the collapse, and the mine will be submerged by the high-pressure water of the coal ash. Therefore, it is particularly important to study the mechanism of the combined effect of high stress on the roof and confined aquifer on the deformation and failure of the coal seam mining floor. This study analyzes and compares the impact of thick-hard magmatic rocks on the destruction of thin floor rock layers in coal seams. Plastic theory calculations are used to determine the plastic zone yield length of floor destruction under hard roof conditions, and the location and height of the maximum floor destruction depth are solved. An empirical formula and BP neural network are used to establish a prediction model for floor destruction. The results of the model's prediction of the depth of floor failure were compared with the measured values, with an absolute error of 2.13 m and a residual of 10.3%, which was closer to the true values. The accuracy of the theoretical model and prediction model is verified using numerical simulation and on-site in situ measurements. Based on this, the deformation and destruction forms of the floor under pressure and the water inrush mechanism are summarized for mining under the condition of a thick-hard roof. Thus, the floor is subjected to high vertical stress, accompanied by significant disturbances generated during coal seam mining, resulting in intense working face pressures. The floor near the working face coal wall will experience severe compression and shear deformation and slide towards the goaf. The floor in the goaf is relieved of high vertical stress, and horizontal stress compression will result in shear failure, leading to floor heave and further increasing the height of the floor destruction zone. After the mining of the working face, the goaf will undergo two stages of re-supporting and post-mining compaction. During the re-supporting stage, the floor rock undergoes a transition from high-stress to low-stress conditions, and the instantaneous stress relief will cause plastic deformation and failure in the coal seam floor. The combined action of primary floor fractures and secondary fractures formed during mining can easily create effective water channels. These can connect to the aquifer or water-conducting structures, making them highly dangerous. The main modes of floor water inrush under the condition of a thick-hard roof are as follows: the high-stress mode, inducing a floor destruction zone connected to the water riser zone; the mining damage mode, connecting to water-conducting faults; the mining damage mode, connecting to water collapse columns; and the coupled water inrush mode, between the mining damage zone and the highly pressurized water floor.

Keywords: thick-hard roof; thin aquifer zone; floor destruction mechanism; under pressure mining

check for updates

Citation: Cao, M.; Yin, S.; Li, S.; Wang, X. Mechanisms of Thick-Hard Roof and Thin Aquifer Zone Floor Destruction and the Evolution Law of Water Inrush. *Water* **2024**, *16*, 2304. https://doi.org/10.3390/w16162304

Academic Editor: Juan José Durán

Received: 17 June 2024
Revised: 2 August 2024
Accepted: 7 August 2024
Published: 15 August 2024

Copyright: © 2024 by the authors. Licensee MDPI, Basel, Switzerland. This article is an open access article distributed under the terms and conditions of the Creative Commons Attribution (CC BY) license (https://creativecommons.org/licenses/by/4.0/).

1. Introduction

The geological and hydrogeological conditions of mines in the Hanxing area of China are complex and intricate, and floor-confined aquifer damage has become one of the most

important factors threatening mine safety production. After more than 70 years of mining, the shallow coal seam resources have been basically exhausted, and the deep lower coal seam has begun to be mined. When mining in deep areas, the distance between the coal seam and the confined aquifer of the Ordovician limestone is small, and the water inrush coefficient is high. If the floor is damaged and the fissures are connected to the aquifer, it will cause major accidents. Due to the high ground pressure, high water pressure, and other conditions in deep mines, as well as the complex faults and collapse columns, the risk of deep engineering has been greatly increased [1]. Many scholars have conducted in-depth and extensive research on the mechanism of floor failure during coal seam mining, and have achieved valuable results, playing an important guiding role in the prevention and control of floor water inrush. The theory of "thin floor structure" is the first to use a simplified condition of thin plate structure to assume the bottom waterproof layer. By calculating the instability strength of the structure, the maximum water pressure that can cause water inrush and the maximum water pressure that the bottom rock layer can withstand are calculated [2–4]. The key layer theory of water inrush from the floor suggests that there is also a critical layer on the aquifer of the floor that can resist loads and determine whether water inrush occurs [5–7]. Water inrush occurs frequently in coal mines, and various prediction methods have been studied to mitigate the damage [8–10]. According to the connection mode of pillar collapse columns and the floor destruction zone, they can be further divided into four sub-modes: thin plate theory sub-mode, shear failure theory sub-mode, thick-walled cylinder water inrush sub-mode, and fracturing water inrush sub-mode [11–13].

The roof and floor conditions of lower-group coal mining in this study area are essentially different from other lower-group coal mining areas in North China. Its particularities are that the coal mining will be subject to high stress from the thick-hard roof and the impact of the floor-confined water, and the coal seam is very close to the Ordovician limestone roof interface. The most difficult problem when studying the mechanism of floor failure involves addressing the damage caused by the thick-hard roof, which does not easily collapse to the floor, while also fundamentally reducing the risk of water inrush from the floor during mining on pressurized water. This involves truly solving the problem of pressure mining on pressurized water. On the basis of previous research results, this paper will explore and discuss the deformation and failure mechanism of floor and water inrush mechanisms under the confined mining conditions of thick-hard roofs and thin floor coal seams.

2. Location and Geological Setup of the Study Area

(1) Overview of the working face in the study area.

The research area is located about 13 km northwest of Wu'an City, China, in the eastern foothills of the Taihang Mountains, as shown in Figure 1. It belongs to the middle and low mountain hilly landform type, with a terrain that is high in the south and low in the north, and high in the west and low in the east. There are eight aquifers (groups) distributed in the mine field, and the hydrogeological profile of the aquifers from bottom to top is shown in Table 1. Among them, the Ordovician limestone aquifer has a large thickness and strong water yield, with a permeability coefficient of up to 31.66 m/d. In the past 10 years, the Ordovician limestone water level has been decreasing year by year, and the current elevation of the Ordovician limestone water level is around + 30 m. The top of the aquifer is 27–40 m away from the coal seam, and the maximum water pressure can reach 2.8 Mpa, which poses a great threat to the mining face. Therefore, it is important to study the deformation and failure characteristics of the floor after coal seam mining in this area. The hydrogeological conditions of the mining area are shown in Figure 2.

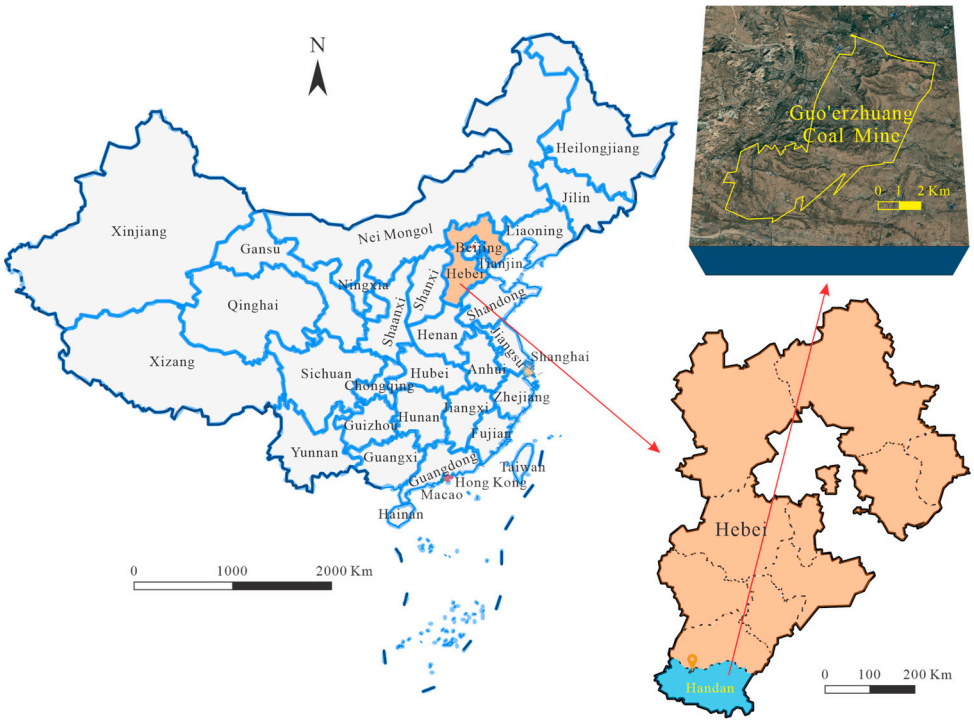


Figure 1. Study area location (China administrative division data from geospatial data cloud).

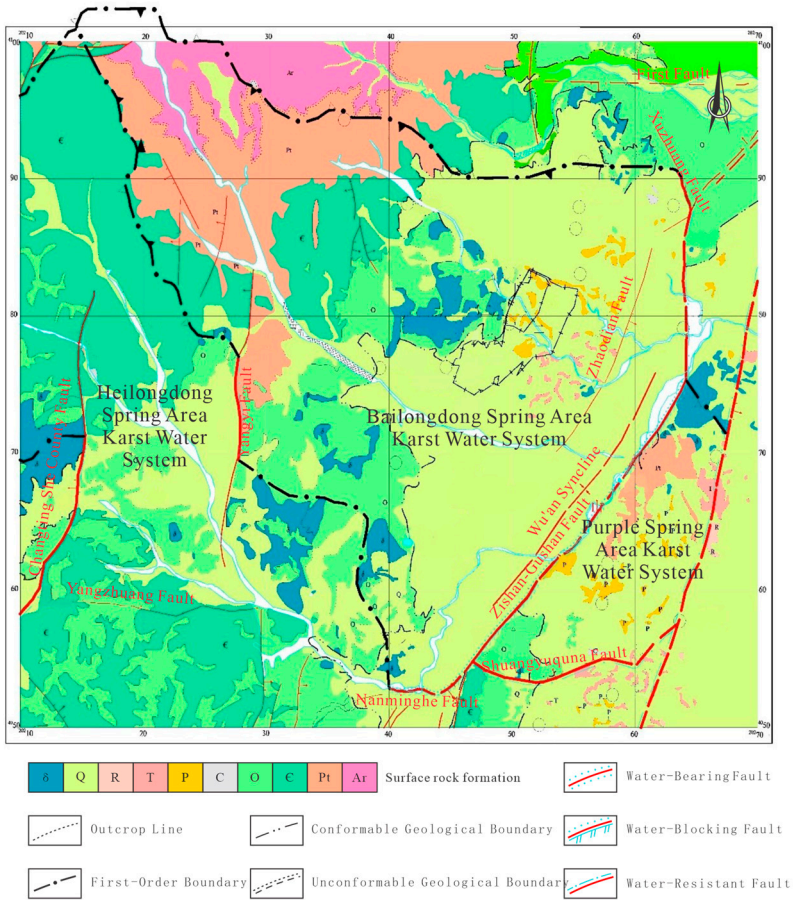


Figure 2. Hydrogeological conditions of mining area.

Table 1. List of characteristics of aquifers in mine fields.

Aquifer	Thickness (m)	Watery	Unit Inflow L/s·m	Water Quality Type
Ordovician limestone karst fissure (I)	600	Strong	North 0.2~85 South 0.1~8.3	HCO_3·SO_4-Ca·Mg
Daqing limestone fissure karst (II)	5.5	Moderate	0.07	HCO_3·SO_4-Mg·NaCa
Fuqing limestone fissure karst (III)	2.5	Moderate	0.1~0.3	
Yeqing limestone fissure karst (IV)	2.1	Weak	0.01~0.02	
Large coal roof sandstone fissure (V)	0.6~16.7	Weak	0.02	
Shihezi Formation sandstone fissure (VI)	40~60	Moderate to weak	0.07~0.1	
Quaternary sand gravel porous (VII)	0~19.6	Moderate to weak	0.7~31.5	HCO_3-Ca
Magmatic rock fissure (VIII)	20~28	Moderate to weak	0.05~0.18	

Statistical analysis of 100 pieces of drilling data from Guo'er Zhuang Mine shows that the 29,205 working face has a burial depth of 251–280 m, with an average depth of 270 m. It primarily mines the ninth coal seam layer, which has a thickness ranging from 1.5 to 3.8 m, with an average thickness of 2.98 m (the distribution of coal seam thickness is shown in Figure 3). The coal seam has a dip angle of 5 to 8 degrees and is classified as a nearly horizontal coal seam. The working face has a strike length of 680 m and a dip length of 70 m. In the upper part of the coal seam, there is a stable interlayer of gangue with an average thickness of 0.84 m. The roof consists of intrusive magmatic rock with an average thickness of 15.27 m, while the immediate floor consists of mudstone and Benxi limestone with an average thickness of 7.65 m. There are no major fault structures in the working face according to the comprehensive stratigraphic column revealed by drilling, as shown in Figure 4.

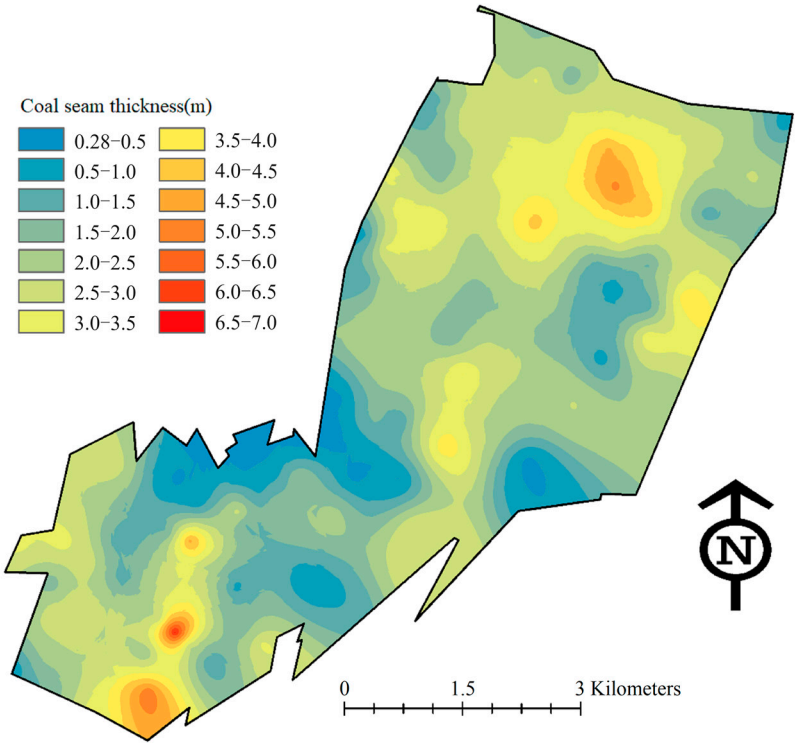


Figure 3. The distribution of coal seam thickness.

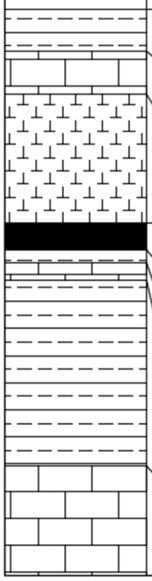
Columnar Structure	Name of Rock Stratum (Coal Seam)	Thickness /m	Description of Rock Stratum Characteristics
	Mudstone	5.18	Black, fine, dense, and containing plant fossils and nodules
	Anthraconite	4.87	Gray, massive, brittle, including animal fossils and calcite veins, cracks developed, local mud
	Dioritic Porphyrite	15.27	Gray, massive structure, hard, crack development, containing calcite veins and massive pyrite, feldspar amphibole-based.
	Coal	2.98	Black-gray, mostly powder-like structure, showing a glass luster, with tonstein
	Mudstone	4.67	Dark-gray, smooth, fine, under the influence of force, joint development, the upper part of the extrusion into a sticky mud
	Benxi Limestone	7.95	Gray, massive structure, containing animal fossils and lumps of pyrite dense, brittle, calcite vein longitudinal
	Mudstone	21.23	Gray, purple-gray alternate, local variegated, horizontal bedding.
	Ordovician Limestone	14.20	Grayish, breccia-like, dense, brittle, partly dolomitic, with lumps of pyrite, crosscut with calcite

Figure 4. Comprehensive stratigraphic column.

(2) Causes and characteristics of the thick-hard roof in the study area

In the research area, the roof of the ninth coal mining layer has been severely intruded by magmatic rocks, with some areas even completely engulfing the coal seam. Magmatic rocks have been found in some areas of the Ordovician limestone layer. The research area is located on the edge of the Jianshan rock mass, which formed during the mid-Yanshan orogeny. During this period, geological movements occurred between the magmatic rocks and the gray mudstone, forming a typical "Handan-Xingtai-style skarn-type magnetite deposit". The magmatic rocks intruded into the fan-shaped Carboniferous strata, causing significant erosion of the Taiyuan Formation. They have an east–west and north–south orientation and exhibit a lenticular and layered distribution in the exposed strata, occasionally showing cross-merging phenomena. The distribution pattern of the upper part of the magmatic rocks is irregular and heterogeneous.

Based on information revealed by multiple boreholes in the study area, the intrusive magmatic rocks can be divided into five layers within the Benxi Formation, with substantial variations in thickness. The thickness generally ranges from 5 to 25 m, with considerable differences between the northern and southern regions. The most severely damaged magmatic rock in the ninth coal mining layer is located between the Benxi Formation and Daqing Limestone. The existence of this layer of magmatic rock changes the rock mechanics parameters of the overlying rock of the coal seam roof, increasing the difficulty of coal seam mining. Its thickness ranges from 2.88 m to 40 m, and it is widely distributed throughout the area, mainly with single-layer intrusion and multi-layer intrusion in some areas. It merges with the upper layer of magmatic rock in the middle of the mine field. The spatial geographic coordinates of this layer of magmatic rock are accurate. The thickness distribution of thick-hard roof magmatic rocks is shown in Figure 5.

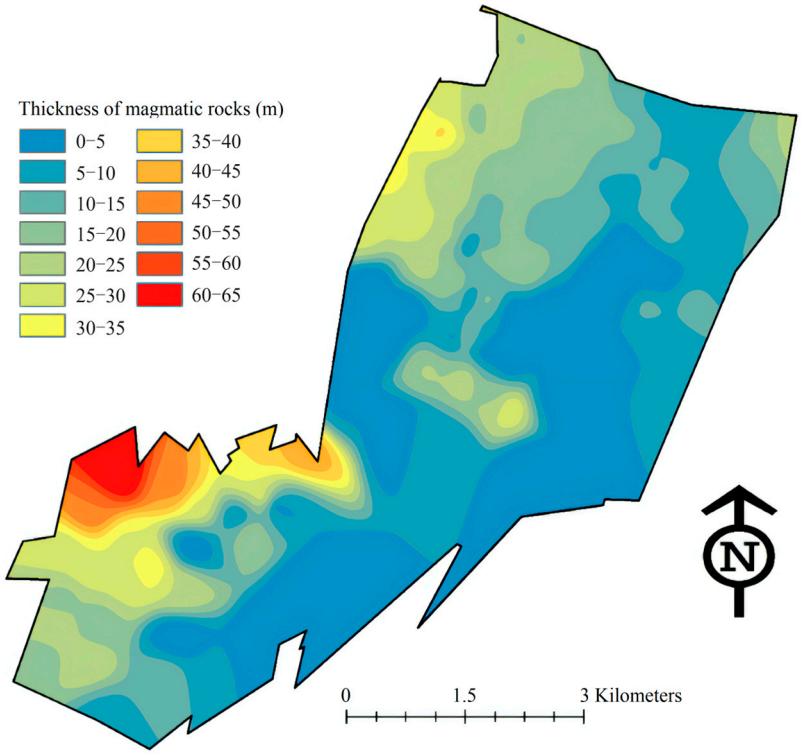


Figure 5. Thickness distribution of magmatic rock in coal seam roof.

3. Mechanism of Floor Destruction and Prediction of the Depth of Floor Damage in Coal Mining with a Thick-Hard Roof

3.1. Plastic Theory for Solving the Depth of Floor Damage

During the coal mining process, once the concentrated stress on the floor exceeds the ultimate strength of the floor rock mass, the floor rock layer undergoes irreversible deformation, transitioning from elastic deformation to creep deformation, and then to plastic deformation until the floor rock mass fractures and generates cracks [14].

(1) Calculation of the maximum depth of floor damage:

In the goaf area, there is a certain free surface, and the rock mass in the creep deformation zone gradually moves towards the goaf area. According to plastic theory, the plastic damage range of the floor can be roughly divided into three zones based on the variation of stress distribution in the rock mass (as shown in Figure 6): Zone (I) is the active stress zone, Zone (II) is the transitional deformation zone, and Zone (III) is the passive stress zone. The slip line (boundary of the plastic deformation zone) of the floor in the active stress zone (I) and the passive stress zone (III) is a straight line, while the slip line of the coal seam floor in the transitional zone (II) takes the form of a "logarithmic spiral" curve, with an equation given by:

$$r = r_0 exp(\theta \tan \varphi_0) \quad (1)$$

In Equation (1):
r—distance between fc (m);
r_0—distance between fd (m);
θ—angle between the r_0 line and r line (°)
φ_0—internal friction angle of the rock mass (°);

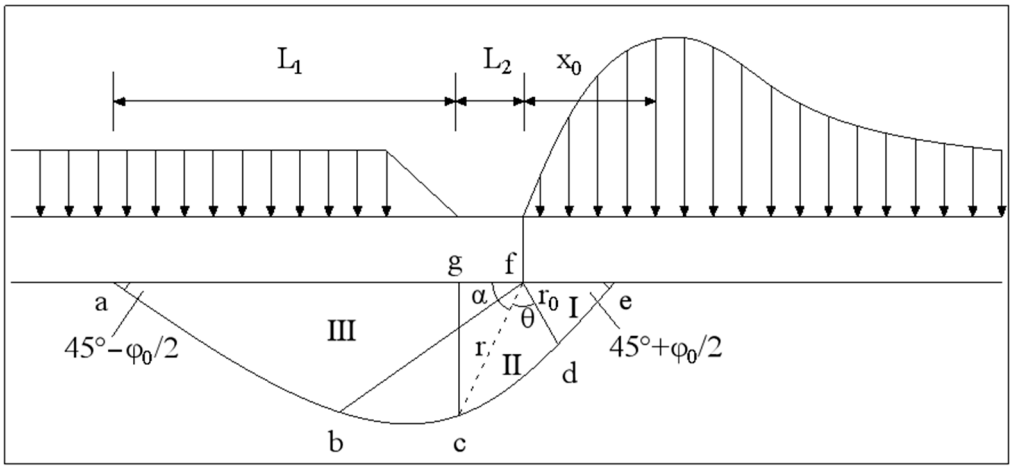


Figure 6. Calculation chart of plastic failure zone of rock mass.

Based on Figure 6, it can be observed that the plastic damage zone of the coal seam floor rock mass, under the influence of the advancing support stress during mining, shows the extent and intensity of the plastic damage.

$$D = rsin\alpha \tag{2}$$

$$D = r_0 exp(\theta tan\varphi_0) sin\alpha \tag{3}$$

$$r_0 = \frac{x_\alpha}{2cos\left(\frac{\pi}{4} + \frac{\varphi_0}{2}\right)} \tag{4}$$

$$\alpha = \frac{\pi}{2} - \theta + \left(\frac{\pi}{4} - \frac{\varphi_0}{2}\right) \tag{5}$$

$$D = r_0 exp(\theta tan\varphi_0) cos\left(\theta + \frac{\varphi_0}{2} - \frac{\pi}{4}\right) \tag{6}$$

x_α—range of coal seam plasticity zone;
θ—failure depth of the mining-induced stress failure zone;
When $\frac{Dd}{d\theta} = 0$, the maximum depth of the failure zone, D_m, can be obtained as follows:

$$\frac{\mathrm{dD}}{\mathrm{d\theta}} = \mathrm{r_0 exp\,(\theta tan\,\varphi_0) cos\left(\theta + \frac{\varphi_0}{2} - \frac{\pi}{4}\right) tan\,\varphi_0 - r_0 exp\,(\theta tan\,\varphi_0) sin\left(\theta + \frac{\varphi_0}{2} - \frac{\pi}{4}\right) = 0} \tag{7}$$

$$\tan\varphi_0 = \tan\left(\theta + \frac{\varphi_0}{2} - \frac{\pi}{4}\right) \tag{8}$$

$$\theta = \frac{\varphi_0}{2} + \frac{\pi}{4} \tag{9}$$

$$D_m = \frac{x_\alpha \cos\varphi_0}{2\cos\left(\frac{\pi}{4} + \frac{\varphi_0}{2}\right)} \exp\left[\left(\frac{\pi}{4} + \frac{\varphi_0}{2}\right) \tan\varphi_0\right] \tag{10}$$

The maximum length of the floor damage along the direction of the working face represents the extent of floor failure in the goaf. In this case, L_1 refers to the maximum floor damage length in the goaf along the direction of the working face.

The distance between the coal wall of the working face and the maximum depth of floor damage in the goaf is represented by L_2. It indicates the minimum value of the distance from the coal wall of the working face to the location of maximum depth of floor damage.

$$L_1 = x_\alpha \tan\left(\frac{\pi}{2} - \frac{\varphi_0}{2}\right) \exp\left(\frac{\pi}{2} \tan\varphi_0\right) \tag{11}$$

$$L_2 = D_m \tan\varphi_0 = \frac{x_\alpha \sin\varphi_0}{2\cos\left(\frac{\pi}{4} + \frac{\varphi_0}{2}\right)} \exp\left[\left(\frac{\pi}{4} + \frac{\varphi_0}{2}\right) tan\varphi_0\right] \tag{12}$$

(2) Calculation of the length of the yielding zone in the coal seam

The length of the yielding zone in the coal seam can be obtained through actual engineering measurements. It can also be calculated using the following formula. Let d_x represent the inclined length of the differential coal unit, and M denote the actual mining thickness of the coal seam. Assuming that the coal–rock mass is in a state of stress equilibrium before mining, the sum of the horizontal stresses along the x-direction is zero, as represented by Equation (13):

$$2(c + \sigma_x \tan\varphi_0)d_x + M\sigma_x - M\left(\sigma_x + \frac{d\sigma_x}{d_x}d_x\right) = 0 \tag{13}$$

$$M\left(\frac{d\sigma_x}{d_x}\right) = 2(c + \sigma_x \tan\varphi_0)d_x \tag{14}$$

At the limit state of coal mass equilibrium, satisfying the Mor–Coulomb criterion can be obtained.

$$\frac{d\sigma_x}{d\sigma_z} = \frac{1}{K_1} \tag{15}$$

$$2(c + \sigma_x \tan\varphi_0) - M\frac{d\sigma_z}{d_x}\frac{1}{K_1} = 0 \tag{16}$$

Solving the differential equation of Equation (16) and substituting the boundary condition $\sigma_x = 0$ when $x = 1$, we can obtain:

During coal seam mining, by substituting the maximum concentrated stress value near the coal wall, σ_z = nyH, into Equation (17), we can obtain the length value of the yielding zone in the coal mass, x_α.

$$\sigma_z = cK_1 cot\varphi_0 exp\left(\frac{2K_1 x tan\varphi_0}{M}\right) - ccot\varphi_0 \tag{17}$$

$$x_\alpha = \frac{M}{2K_1 tan\varphi_0} ln\frac{n\gamma H + ccot\varphi_0}{K_1 ccot\varphi_0} \tag{18}$$

In equations:
H—burial depth of the coal seam in meters (m);
x_α—length value of the yielding zone in the coal mass in meters (m);
M—working face mining height in meters (m);
c—cohesion of the coal seam (MPa);
φ_0—internal friction angle of the coal seam (°).

$$K_1 = \frac{1 + \sin\varphi_0}{1 - \sin\varphi_0} \tag{19}$$

$$x_\alpha = 0.015H \tag{20}$$

Drawing on the modification of the empirical formula for the length of the yielding zone in coal by A.H. Wilson, we obtain Equations (21) and (22):

(1) When the physical and mechanical strength of the rock mass (roof and floor) above and below the coal seam is higher than that of the coal seam.
(2) When the physical and mechanical strength of the rock strata above and below the coal seam is close to that of the mining coal seam.

$$x_\alpha = \frac{M}{F}\ln(10\gamma H) \tag{21}$$

$$x_\alpha = \frac{M}{2}\left[(10\gamma H)\frac{1}{K_1 - 1} - 1\right] \tag{22}$$

$$F = \frac{K_1 - 1}{\sqrt{K_1}} + \left(\frac{K_1 - 1}{\sqrt{K_1}}\right)^2 \arctan\sqrt{K_1} \tag{23}$$

Taking the given values into account, with the average burial depth of the coal seam (H) being 270 m, the average mining height (M) being 3 m, the average apparent density of the rock layers (γ) from the working face roof to the surface being 2500 KN/m^3, the measured internal friction angle of the mining coal seam (φ) being 25°, and the average internal friction angle of the water-bearing layer below the coal seam (φ_0) being 35°, we can substitute these parameters into Equation (19) to obtain Equation (24):

By substituting the result of Equation (24) into Equation (23), we obtain Equation (25):

$$K_1 = \frac{1 + sin\varphi}{1 - sin\varphi} = \frac{1 + sin25}{1 - sin25} = 2.46 \tag{24}$$

$$F = \frac{K_1 - 1}{\sqrt{K_1}} + \left(\frac{K_1 - 1}{\sqrt{K_1}}\right)^2 \arctan\sqrt{K_1} = \frac{2.46 - 1}{\sqrt{2.46}} + \left(\frac{2.46 - 1}{\sqrt{2.46}}\right)^2 arctan\sqrt{2.46} = 2.52 \tag{25}$$

As shown in Figure 7, the length of the yielding zone in the coal seam, x_α, is given by Equation (26). The maximum depth of floor damage in the rock layer, D_m, is given by Equation (27). The minimum horizontal distance between the location of the maximum depth of floor damage in the goaf and the coal wall along the direction of the working face is calculated as shown in Equation (28). The extent of floor damage in the goaf is represented by Equation (29).

$$x_\alpha = \frac{M}{2}\left[(10\gamma H)\frac{1}{K_1 - 1} - 1\right] = \frac{3}{2}\left[\left(10 \times 2500 \times 270/10^6\right) \times \frac{1}{2.52 - 1} - 1\right] = 5.16m \tag{26}$$

$$D_m = \frac{x_\alpha \cos\varphi_0}{2\cos\left(\frac{\pi}{4} + \frac{\varphi_0}{2}\right)} \exp\left[\left(\frac{\pi}{4} + \frac{\varphi_0}{2}\right)\tan\varphi_0\right] = 15.3\mathrm{m} \tag{27}$$

$$L_2 = D_m \tan\varphi_0 = \frac{x_\alpha \sin\varphi_0}{2\cos\left(\frac{\pi}{4} + \frac{\varphi_0}{2}\right)} \exp\left[\left(\frac{\pi}{4} + \frac{\varphi_0}{2}\right) tan\varphi_0\right] = 10.71 \tag{28}$$

$$L_1 = x_\alpha \tan\left(\frac{\pi}{2} - \frac{\varphi_0}{2}\right) \exp\left(\frac{\pi}{2}\tan\varphi_0\right) = 111.7 \tag{29}$$

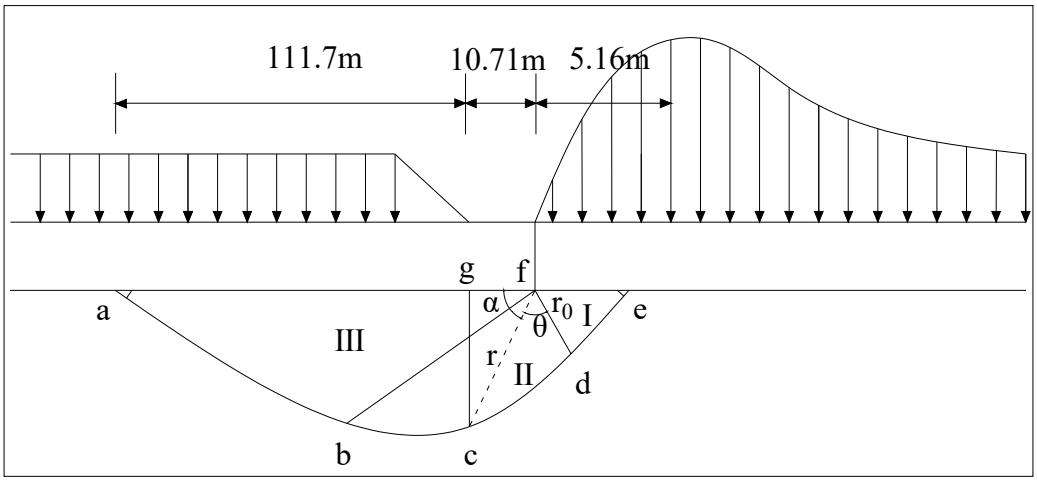


Figure 7. Schematic diagram of the failure form of the floor in the goaf.

3.2. Calculating the Depth of Floor Damage Using Standard Empirical Formulas

In the 'Code for Design on Pillar Reserving and Pressure Coal Mining of Buildings, Water Bodies, Railways, and Major Tunnels' (hereafter referred to as the code), a large number of observed values of floor damage depth are statistically analyzed. Using the linear regression method, factors influencing the depth of floor damage, such as the inclined length of the working face, coal seam mining depth, coal seam mining thickness, and

working face inclination angle, are taken into consideration. Accordingly, the code presents the following statistical formula.

When considering only the inclined length of the working face, the maximum depth of the floor damage zone can be determined using Equations (30) and (31). When considering the coal seam mining depth, coal seam mining thickness, and inclined length of the working face, the depth of the floor damage zone can be calculated using Equation (32).

$$h_1 = 0.7007 + 0.1079L \tag{30}$$

$$h_1 = 0.303L^{0.8} \tag{31}$$

$$h_1 = 0.0085H + 0.1665\alpha + 0.1079L - 4.3579 \tag{32}$$

In these equations:
h_1—depth of the floor damage zone in meters (m);
L—length of the retreating working face in meters (m);
H—mining depth in meters (m);
α—coal seam inclination angle (°).

By substituting all the parameters of the test working face into Equation (32), the depth of the floor damage zone is calculated to be 7.73 m.

3.3. Deep Learning-Based Prediction of Floor Damage Depth Using a BP Neural Network

There are many factors that affect the depth of coal seam floor damage, and the relationship between each factor and the depth of damage is nonlinear. A BP neural network is an artificial intelligence algorithm that has strong nonlinear mapping ability, self-learning, self-organization, and adaptive ability. This method can automatically adjust its internal parameter weights and bias parameters to minimize errors and efficiently process different types of datasets, demonstrating excellent performance in solving complex problems such as nonlinear variations. Compared with traditional machine learning methods, this method requires less manual intervention and can extract effective information from raw data for classification and regression training analysis. It is simple to operate, easy to implement, and has universal applicability.

(1) The Creation of BP Neural Network Model

The learning process of the BP neural network can be mainly divided into two steps: (1) forward propagation of working signals, and (2) backward propagation of error signals [15,16]. The learning structure diagram of the BP neural network is shown in Figure 8.

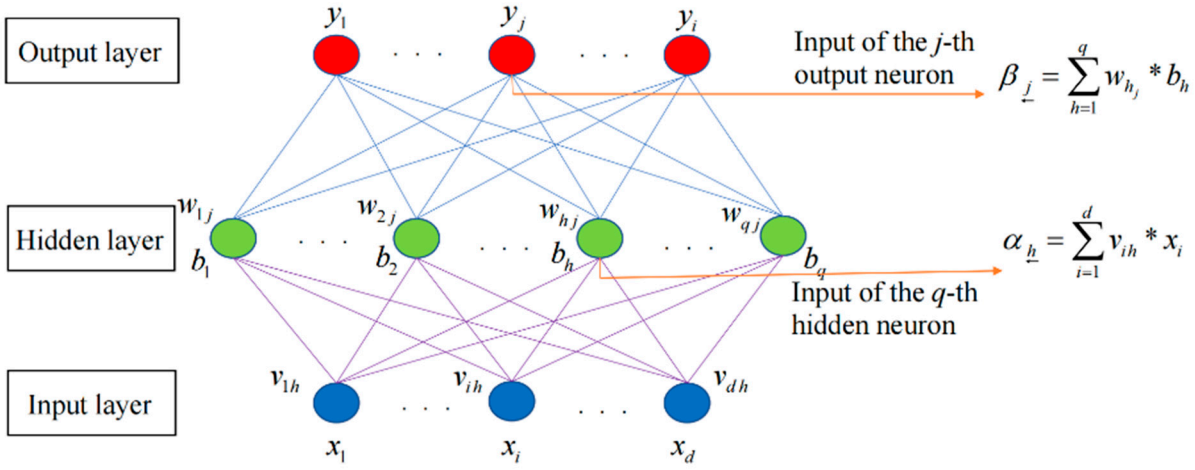


Figure 8. Schematic diagram of BP neural network structure.

Based on the principles of selecting data for the input layer of the BP neural network, the influencing factors of floor damage depth in the coal seam are quantitatively analyzed. A total of 100 different measurements of floor damage depth in coal mine working faces were collected from 23 reference papers, as shown in Table 2. The detailed data, including mining depth, coal seam inclination angle, mining thickness, length of the retreating working face, whether there are structures crossing, and floor damage depth, were used as training and validation samples for the prediction model. The first 70 samples (samples 1–70) were used as the learning samples for training, while the remaining 30 samples were used as the validation samples for verification [17]. The sample data is sourced from the following references [15,18–39].

Table 2. Training and verification samples.

Serial Number	Working Face Number	Mining Depth/m	Dip Angle/°	Mining Thickness/m	Working Face Length/m	Geological Structure	Maximum Damage Depth of the Bottom Plate/m	Data Source
1	Wangfeng coal mine 1830	123	15.0	1.10	70	No	7.0	[15]
…	…	…	…	…	…	…	…	
30	Wucun coal mine 3305	327	12.0	2.40	120	No	11.7	
31	Luling coal mine II 1018	560	20.0	2.25	-	No	13.6	[18]
32	Luling coal mine II 1020	580	20.0	2.25	-	No	16.9	
33	Chensilou coal mine 21301	584	10.0	2.70	149	No	14	[19]
…	…	…	…	…	…	…	…	
37	Dongpang coal mine 9103	237	12.0	6.19	70	No	12.43	
38	Caozhuang coal mine 8812	420	20.0	1.97	120	No	18.5	[20]
39	Caozhuang coal mine 9604	315	17.0	1.35	120	No	14.2	
40	Shuanggou coal mine 1204	308	15.0	1.40	135	No	10.5	[21]
41	Fenxihe coal mine	379	3.0	3.60	180	No	17.3	[22]
…	…	…	…	…	…	…	…	
45	Liuqiao coal mine	450	9.0	1.90	170	No	21	
46	Gequan coal mine	240	10.0	5.30	75	No	12.5	[23]
47	Coal mine 01658	291	7.0	3.67	240	No	26.6	[24]
48	Xiegou coal mine 18102	348	5.0	5.80	225	No	32	[25]
49	Coal mine	200	10.0	1.60	100	No	10.7	[26]
50	Yangmei No.5 coal mine 8403	520	8.5	8.74	220	Yes	20	[27]
…	…	…	…	…	…	…	…	
64	Xing Dong coal mine 2121	1000	12.0	3.70	150	No	32.5	
65	Guandi coal mine 22611	679	6.0	2.99	220	No	27.08	[28]
…	…	…	…	…	…	…	…	
74	Zhenchengdi coal mine 28103	308	11.0	4.50	115	No	12.5	
75	9101	336	6.0	1.34	100	No	15.32	[29]
…	…	…	…	…	…	…	…	
80	8203	468	7.0	1.93	85	No	27.44	
81	Changping coal mine 5302	470	8.0	4.40	300	No	18.7	[30]
82	Longwanggou coal mine 61601	370	5.0	23.0	225	No	18.2	[31]
83	Baode coal mine 81306	700	4.0	2.10	260	No	14.1	[32]
84	Dongjiahe coal mine	500	6.0	3.00	114	No	10.8	[33]
85	Longmen coal mine	300	18.0	4.00	100	No	14	[34]
86	Dongjiahe coal mine #5507	330	6.0	3.71	114	No	10.8	[35]
87	Liuqiao No.1 coal mine 663	695	12.0	2.66	200	No	18.88	[36]
88	Qingdong coal mine	489	15.0	2.75	320	No	16.86	[37]
89	Liudian coal mine	660	13.0	3.50	200	No	15	
90	Pansan coal mine 12318	590	14.0	3.00	205	No	24.6	
91	Zhangji coal mine 1612A	540	9.5	6.30	200	No	28	[38]
…	…	…	…	…	…	…	…	
99	1611A	500	9.0	6.80	215	No	28	
100	Dongqu coal mine	178	5	3.44	220	No	7.06	[39]

During the training process, five input vectors representing the influencing factors of floor damage depth in the coal seam were set in the input layer, including mining depth, coal seam inclination angle, length of the working face, coal seam thickness, and whether there are structures. A total of three layers were set in the neural network, including two hidden layers and one output layer. Each hidden layer contained five neurons. The Tansig function was chosen as the transfer function for the two hidden layers, and the Purelin function was chosen as the transfer function from the hidden layers to the output layer. The learning function used was Trainrp, with a learning rate assigned as 0.05 and the number of learning iterations set to 60,000 [21,40–42]. The training grid and convergence result of the BP neural network is shown in Figure 9.

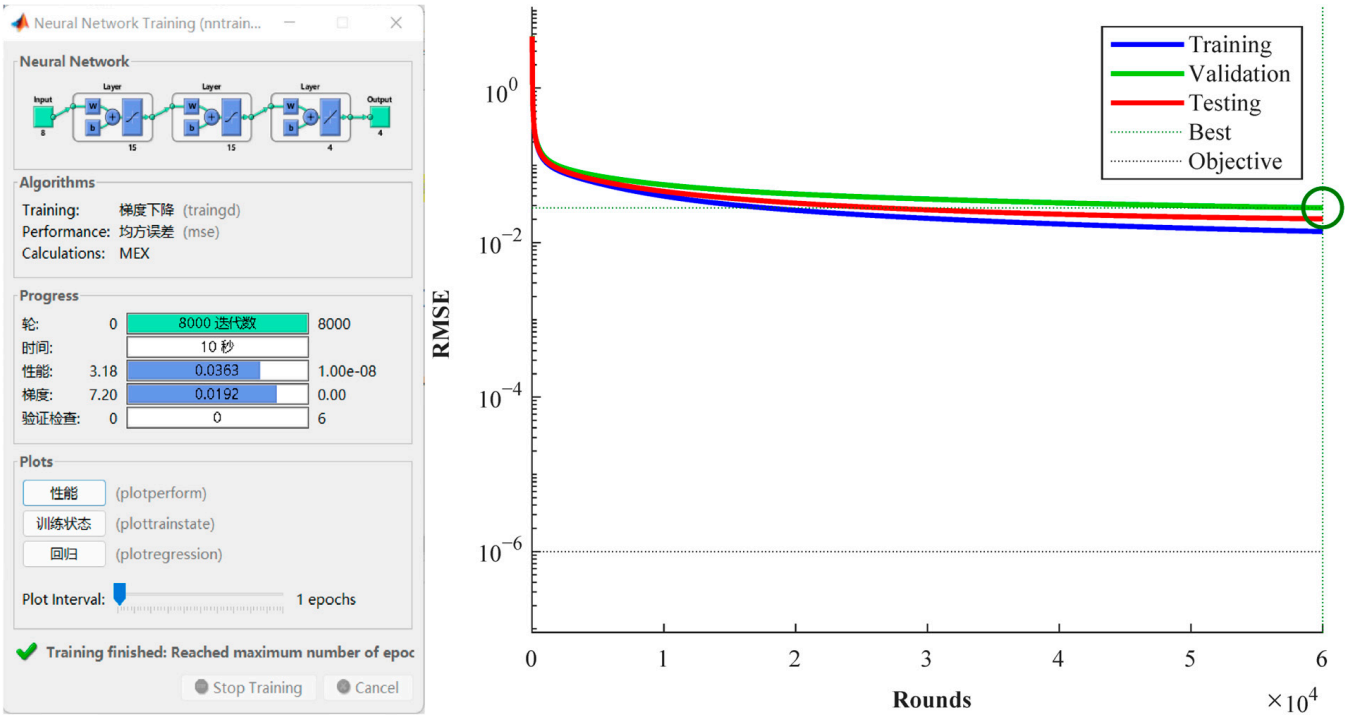


Figure 9. Training result of BP neural network.

From Figure 9, it can be observed that after 60,000 iterations of training, both the training and validation samples have reached the set minimum error. The neural network achieves the minimum RMSE (Root Mean Squared Error) with a convergence value of 0.0028162, indicating an ideal performance.

(2) Analysis of the Results of the Floor Damage Depth Prediction Model

From Figure 10a, assuming that the true values and predicted values are perfectly aligned in an ideal scenario, all 30 samples would fall on a diagonal line with a slope of 1. In reality, the scatter plot of the 30 validation samples is distributed near the diagonal line. The correlation coefficient R is 0.9677, and the coefficient of determination R^2 is 0.9363. Based on previous training experience, a determination coefficient exceeding 0.85 indicates a good fit. Therefore, this prediction model demonstrates excellent performance and a highly accurate fit.

From Figure 10b, this percentage indicates the difference between the predicted values and the true values relative to the true values. From the graph, we can observe that the maximum relative error is 11%, while the minimum relative error is 0%. Furthermore, approximately 83.3% of the validation samples have a relative error within 5%. This demonstrates that the predicted values for the validation samples have very small errors.

From Figure 10c, it can be observed that the maximum error between the predicted and true values for the validation samples is ±6 m, while the minimum error is 0. Approxi-

mately 83.3% of the validation samples have errors within ±2 m. This indicates that the prediction model performs excellently, with a high level of accuracy in predicting the floor damage depth. It can be observed that 66.6% of the samples have residuals distributed within ±1, while 83.3% of the samples have residuals distributed within ±2. Furthermore, 93.3% of the samples have residuals distributed within ±4, and all 100% of the samples have residuals within ±6. This indicates that the floor damage depth prediction model exhibits an excellent performance, as demonstrated by the residual distribution of the validation samples.

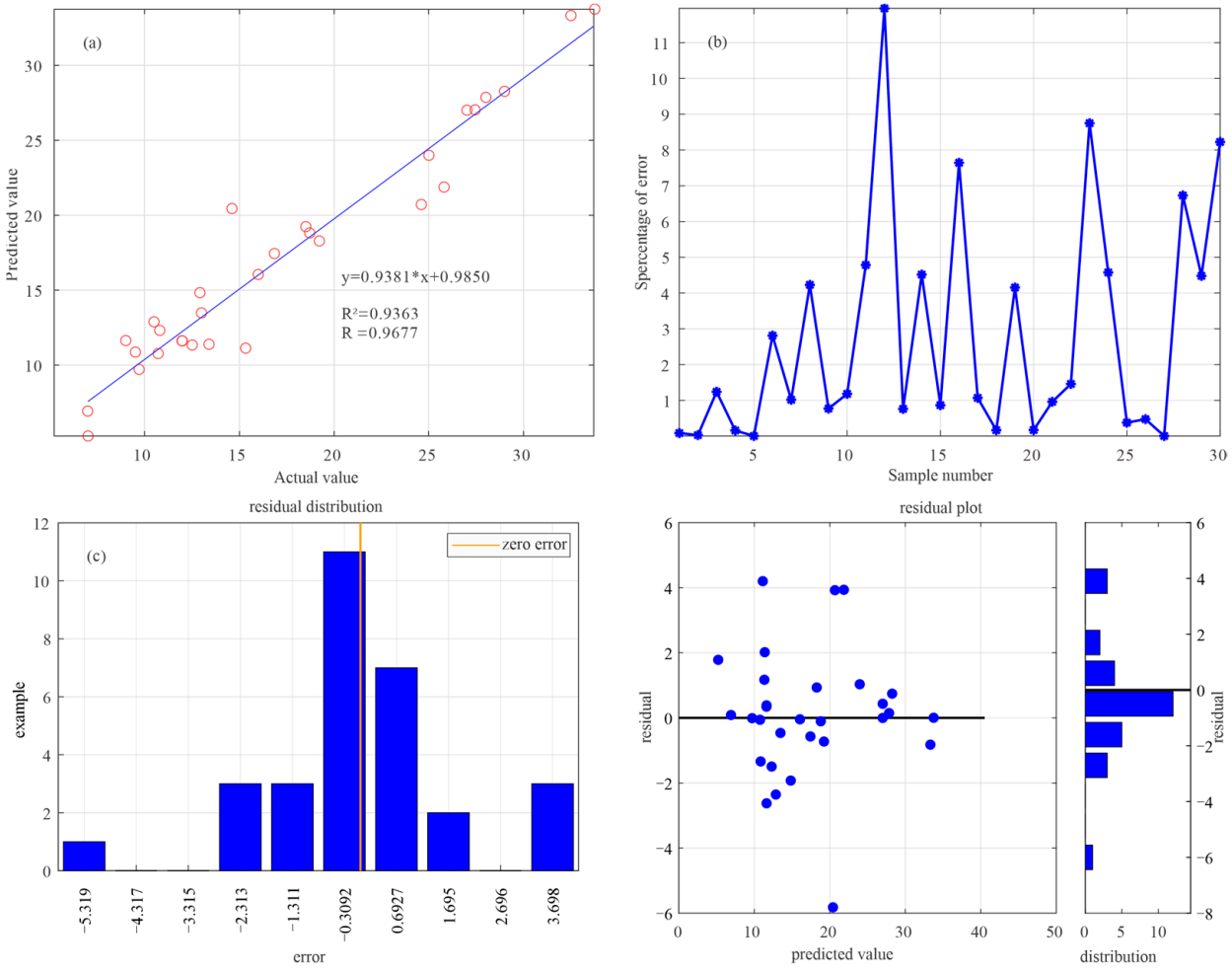


Figure 10. Analysis prediction results of BP neural network model. (**a**) Comparison between predicted and true values of validation samples. (**b**) Verify the relative error between the predicted value and the real value of the sample. (**c**) Verify sample residuals and residuals distribution.

When we input the parameters from Guo'er Zhuang working face 29205—a mining depth of 270 m, coal seam thickness of 3 m, working face length of 70 m, coal seam inclination angle of 7°, and no fault structure—into the BP neural network depth learning model for floor damage depth prediction, we obtain a predicted floor damage depth of 18.57 m for the coal seam.

3.4. FLAC3D Numerical Simulation Calculate the Depth of Floor Damage and Investigate the Pattern of Damage

(1) Model Establishment

Based on the actual geological data of the coal seam excavation and the physical–mechanical parameters of the roof and floor rocks determined in the laboratory, a FLAC3D

mining model is established. The aim is to ensure that the mechanical structure of the model conforms to the actual conditions. By analyzing the stress field, displacement field, and plastic zone resulting from coal seam excavation, the damage mechanism and patterns of the roof and floor after excavation are obtained. This provides reliable data support for studying the mechanism of floor damage [43,44].

A numerical simulation model is established based on the extraction conditions of Guo'er Zhuang coal mine working face 29205. The coal seam has a burial depth of 270 m, mining height of 3 m, inclination angle of 6°, and working face length of 80 m. The numerical model is simplified to 23 layers, with 18 layers for the roof and 5 layers for the floor. The model spans a length of 600 m in the strike direction and 400 m in inclination direction. The *x*-axis represents the strike direction (advancing direction) of the working face, the *y*-axis represents the inclination direction, and the *z*-axis represents the vertical direction (gravity direction) with positive values pointing upward (as shown in Figure 11). Normal constraints are applied to the four sides of the model, and a vertical fixed constraint is imposed on the bottom. The roof is subjected to stress loads corresponding to the distance between the top boundary of the model and the surface [11,43,44].

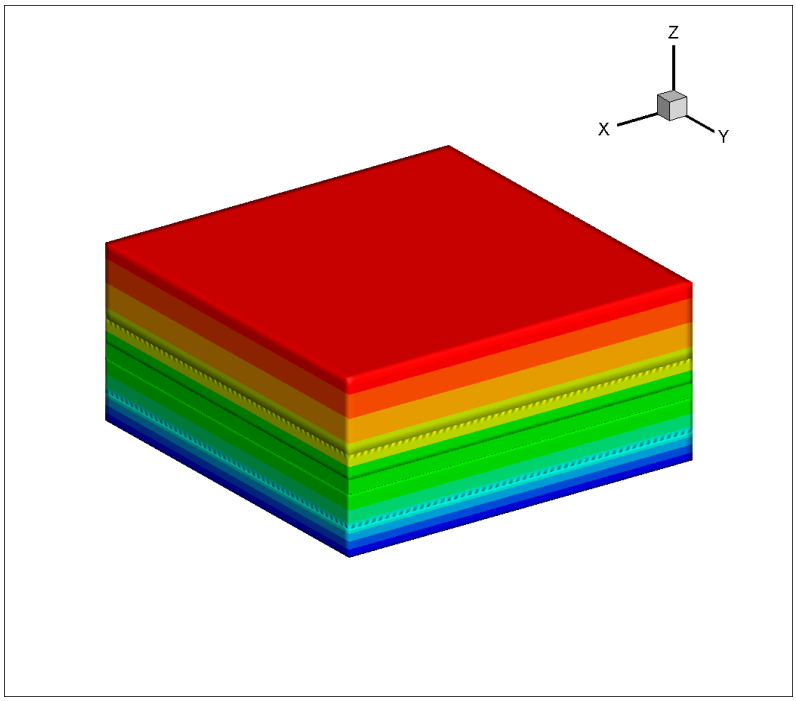


Figure 11. The 29205 working face 3D model.

During the excavation process of the entire model, in order to better reproduce the stress state around the working face, working face 29201 and working face 29203 are first excavated before the excavation of working face 29205. The three working faces have the same length of 80 m, and there is a 5 m interval between each working face as protection pillars based on the actual situation. The mining height is set to 3 m, and the entire thickness of the coal seam is extracted in one operation. The roof management adopts the method of complete collapse. In the FLAC3D simulation, the working face advances 20 m in the advancing direction in each step. A total of 25 steps are simulated, resulting in a cumulative simulated length of 500 m.

Before solving the excavation of the model, boundary conditions must be applied. The nodal velocities and stresses of all elements are set to 0. Lateral constraints with progressively decreasing initial stresses are applied to the four lateral faces. The bottom is subjected to fixed stress load constraints. The entire rock mass is assigned an equivalent gravitational acceleration. Boundary displacements are controlled by nodal velocities, and

initial equilibrium states are set to ensure force balance at the element nodes. At this point, the model construction is complete [38,45].

(2) Analysis of Model Excavation Results

1. Stress Variation Characteristics of the Rock Mass

To clearly illustrate the changes in stress of the roof and floor surrounding rocks throughout the entire excavation process, stress contour plots are plotted at distances of 40 m, 80 m, 120 m, 160 m, 200 m, 240 m, 280 m, 320 m, 360 m, and 400 m along the advancing direction, as shown in Figure 12. As the simulated working face continues to advance and the length of the working face extraction increases, we can observe from the figures that there is a zone of stress concentration near the fully mechanized working face. When working face 29205 is excavated to a distance of 40 m along the advancing direction, neighboring working faces have been fully extracted, resulting in relatively high support pressure acting on the working face. The roof and floor of the working face are in an area of increased mining-induced stress, with the most concentrated moving support stress occurring at the ends of the roadway. As the longwall face advances to the 80 m position, the concentrated mining-induced stress increases with the increasing advancing distance. The maximum vertical stress concentration reaches up to 38 MPa, while the most concentrated moving support stress area remains at the sides of the roadway. As the advancing face continues to progress, the area of the goaf increases, and the concentrated mining-induced stress near the coal wall also increases. When the face advances to the 120 m position, the maximum stress value reaches 40 MPa. As the face progresses to 160 m, the maximum vertical stress no longer continues to increase significantly and tends to flatten out, reaching a maximum value of 40 MPa. As the face advances to 400 m, the maximum vertical stress reduces slightly, with a maximum value of 32 MPa.

2. Displacement Variation Characteristics of the Rock Mass

As shown in Figure 13, it can be observed that as the working face continues to advance, significant displacement occurs in the roof due to the excavation of the coal seam and continuous overburden pressure. However, because the roof is a thick and hard magmatic rock mass, the displacement of the roof and floor does not significantly increase as the face advances, with an increase of only 17 cm to 18 cm from the beginning to the end. In the simulation process, as no progressive load is applied to the bottom interface, the displacement of the floor ranges from 3 cm to 12 cm, with the maximum displacement occurring consistently in the middle of the goaf.

3. Plastic Zone Variation Characteristics of the Roof and Floor

As shown in Figure 14, during the face advancement process, due to the high vertical stress near the coal wall, significant tensile–shear failure occurs in the floor near the coal wall, with shear failure being the main mechanism. When the face reaches the 120 m position, the roof exhibits a distinct "saddle" distribution, while the floor shows an inverted "saddle" distribution. As the face advances to 160 m, there is no significant increase in the depth of floor damage, reaching its maximum value, while the plastic zone continues to expand in the roof, reaching its maximum height at the 320 m position. As the face advances, the coal wall is subjected to pressure from the overlying strata and water pressure from the floor, resulting in an increase in the depth of mining-induced damage. Weak zones in the floor water-bearing layer are prone to develop secondary fractures, forming effective water drainage channels. Pressurized water enters the mining-induced damage zone through these channels and reaches the working face, potentially inducing floor water inrush disasters.

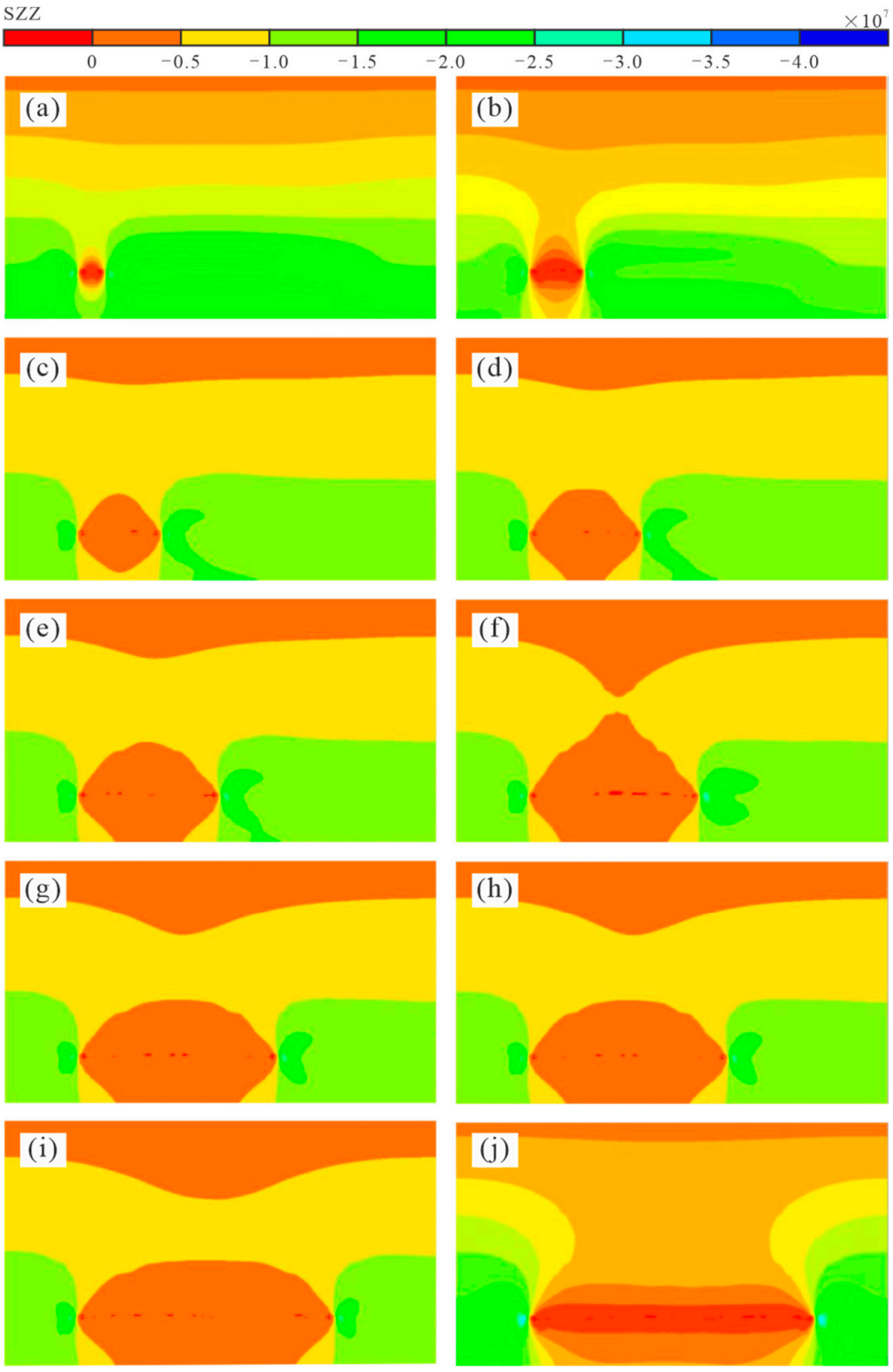


Figure 12. Contour map of vertical stress change of the roof and floor rock mass when the working face is mined to 400 m along the strike. (**a**) excavation 40 m; (**b**) excavation 80 m; (**c**) excavation 120 m; (**d**) excavation 160 m; (**e**) excavation 200 m; (**f**) excavation 240 m; (**g**) excavation 280 m; (**h**) excavation 320 m; (**i**) excavation 360 m; (**j**) excavation 400 m.

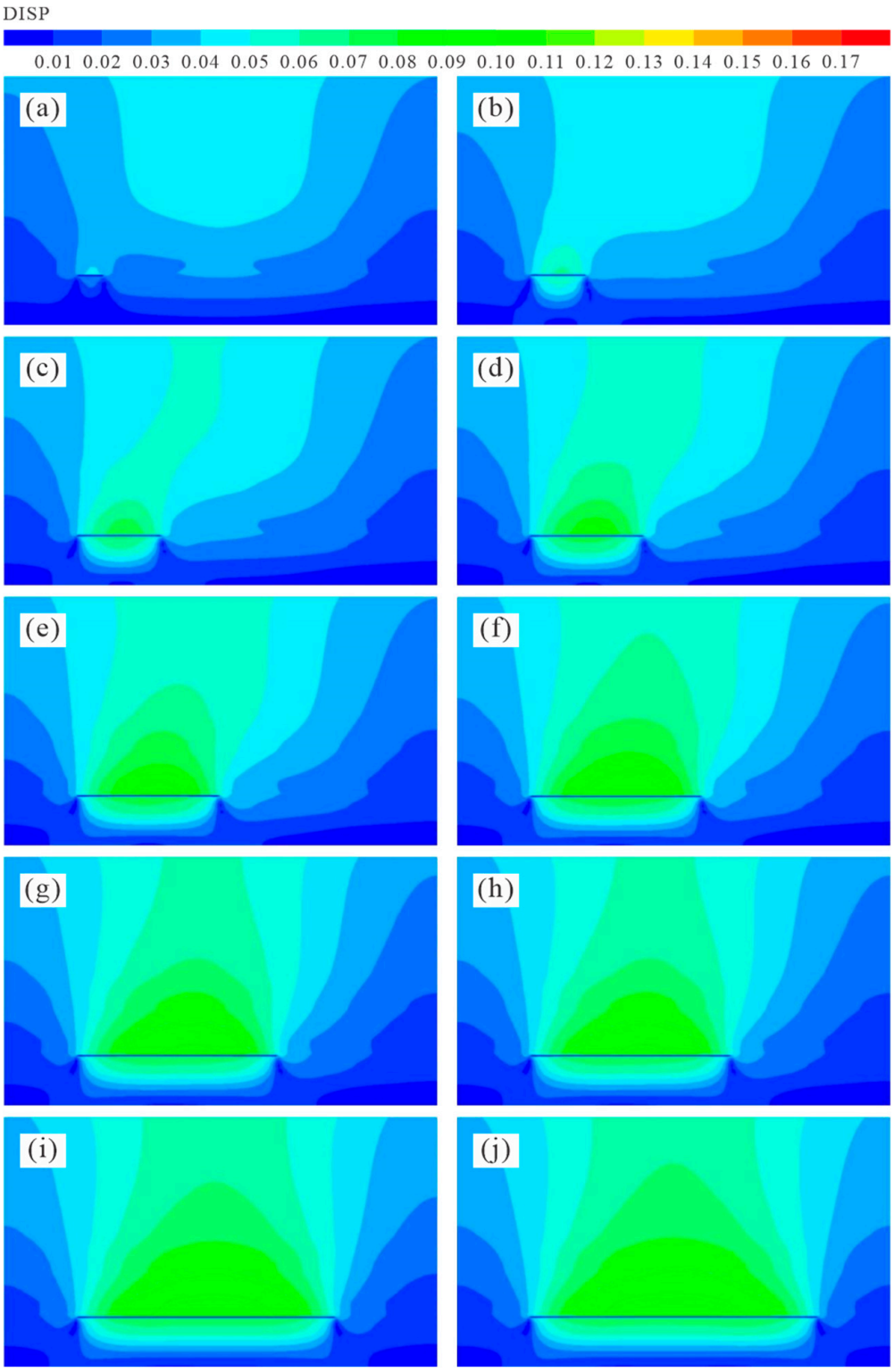


Figure 13. Contour map of displacement change of the roof and floor rock mass when the working face is mined to 400 m along the strike. (**a**) excavation 40 m; (**b**) excavation 80 m; (**c**) excavation 120 m; (**d**) excavation 160 m; (**e**) excavation 200 m; (**f**) excavation 240 m; (**g**) excavation 280 m; (**h**) excavation 320 m; (**i**) excavation 360 m; (**j**) excavation 400 m.

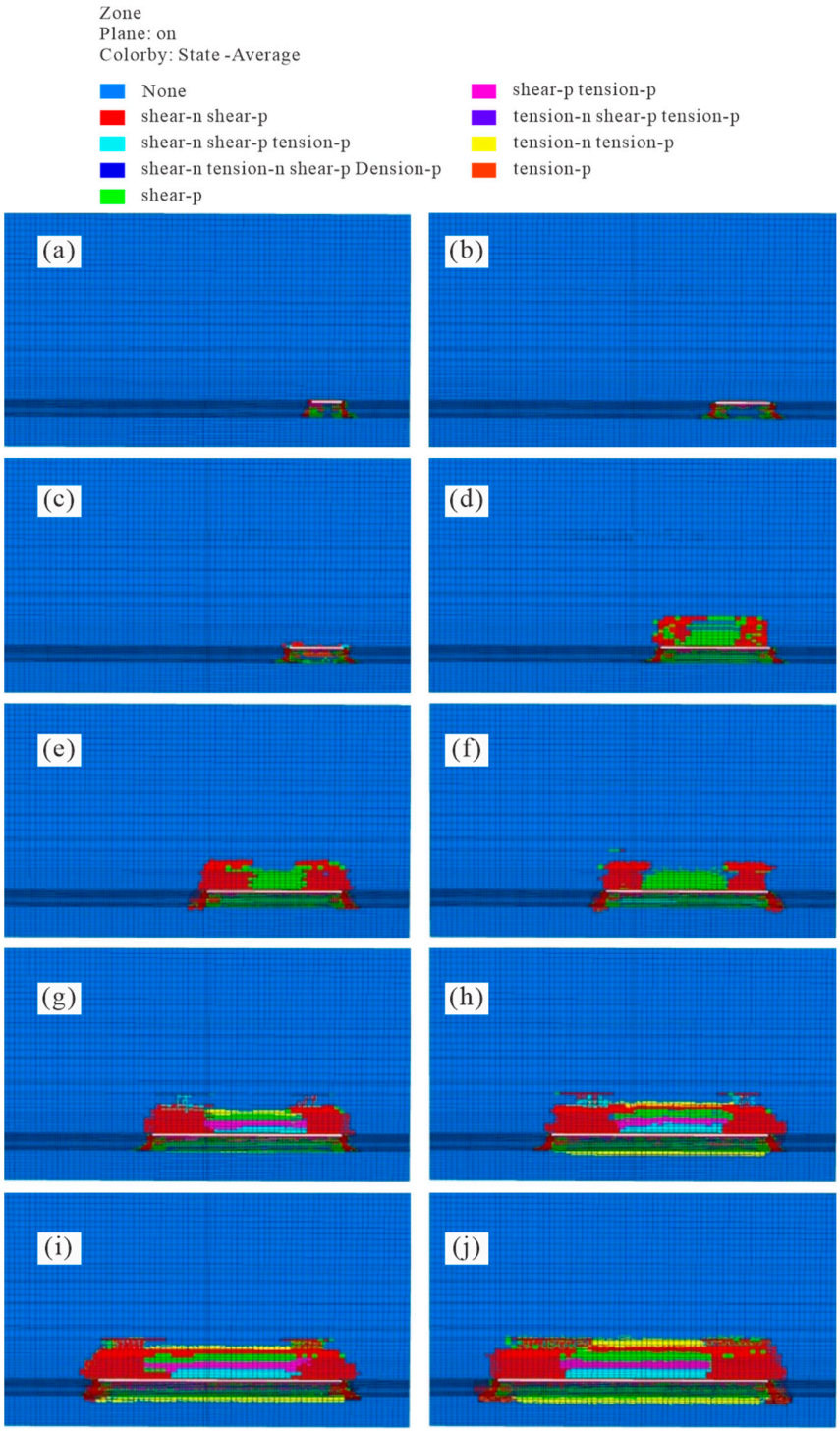


Figure 14. Contour map of the plastic zone distribution of the roof and floor rock mass when the working face is mined to 400 m along the strike. (**a**) excavation 40 m; (**b**) excavation 80 m; (**c**) excavation 120 m; (**d**) excavation 160 m; (**e**) excavation 200 m; (**f**) excavation 240 m; (**g**) excavation 280 m; (**h**) excavation 320 m; (**i**) excavation 360 m; (**j**) excavation 400 m.

3.5. In Situ Measurements of Floor Damage Depth in a Working Face with a Thick-Hard Roof Overlaying Rock Mass Have Been Conducted

(1) Current Measurement Equipment and Principles

There are various methods available for measuring floor damage depth, including the representative methods of segmented water injection test (confined aquifer test), direct

current method, and acoustic CT detection. Considering the hydrogeological conditions of working face 29205 in the Guo'er Zhuang coal mine, a segmented water injection method is employed for in situ measurement of the coal seam floor damage depth. The segmented water injection method involves drilling inclined boreholes from the side entries or chambers on both sides of the working face, with the depth of the boreholes surpassing the anticipated maximum depth of floor damage by a certain distance. The operation steps and equipment details of the drilling double stage water stopper can be found in reference [46].

(2) Field In situ Drilling Layout Plan

To observe the floor damage depth of the southern wing working face, three sets of boreholes are arranged in the return air heading of working face 29205. Each set includes two monitoring points. Specifically, D01 and D02 boreholes are positioned with an azimuth angle of 90° to observe the bottom damage depth of the 29203 working face. D03 and D04 boreholes are positioned at an azimuth angle of 270° to observe the degree of primary fracture development in the working face 29205. D05 and D06 boreholes are positioned at an azimuth angle of 200° to observe floor damage during the mining process of the working face 29205, as shown in Figures 15 and 16. Subsequently, confined aquifer tests are conducted using double-end water-blocking devices in the boreholes to infer the development of rock fractures, facilitating the control of the maximum depth of floor damage.

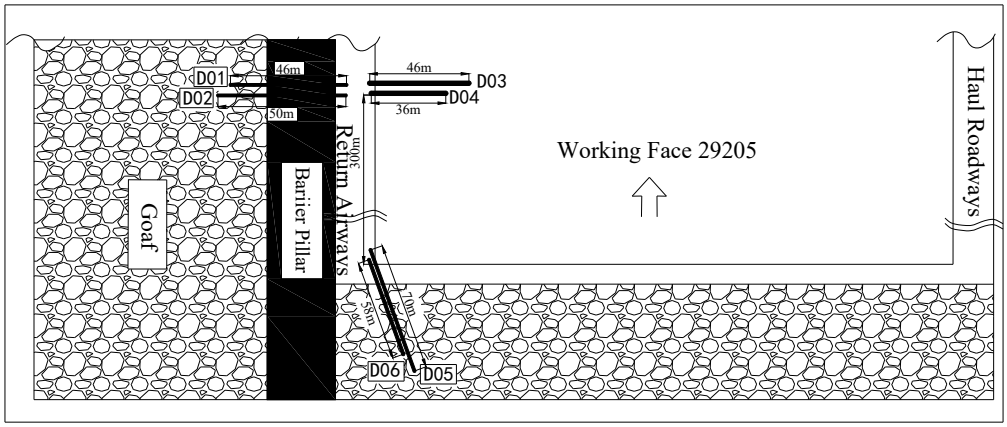


Figure 15. Drilling double stage water stopper layout plan.

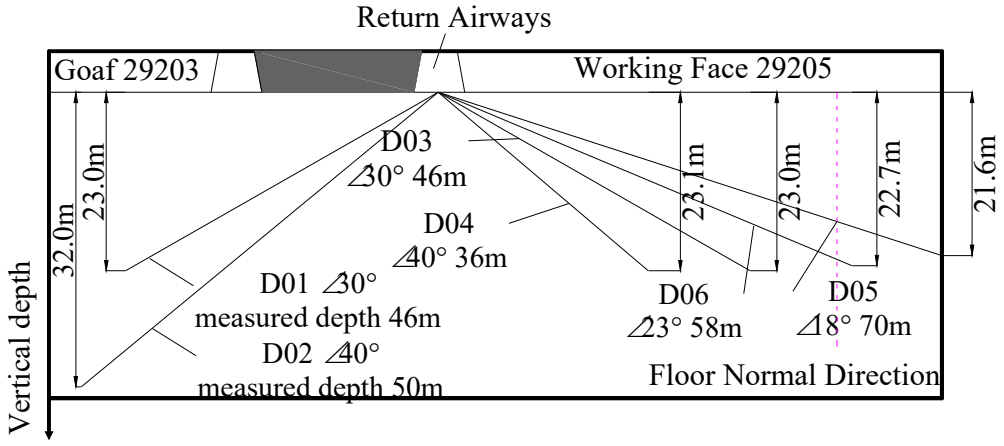


Figure 16. Drilling double stage water stopper layout sections.

(3) In situ Measurement Results and Analysis of Maximum Floor Damage Depth

Plastic failure of the coal seam floor is a progressive deterioration process. Initially, the stress slowly increases, leading to gradual elastic deformation. When the stress reaches the critical value for plastic failure, the floor rock fractures, and the development of fractures within the rock mass results in the loss of water resistance in the fractured section of the floor water-bearing layer. Therefore, it is reasonable to analyze floor damage through the observation of water leakage during water injection tests. Based on the in situ measurement data, a cylindrical plot of water leakage in the boreholes is generated to observe the depth of floor damage. The horizontal axis below represents the inclined depth of the boreholes entering the floor, the horizontal axis above represents the vertical height of the boreholes from the floor, and the vertical axis represents the water leakage rate per unit time in the boreholes. The curves of water leakage for the boreholes (D01–D06) are shown in Figures 17–19.

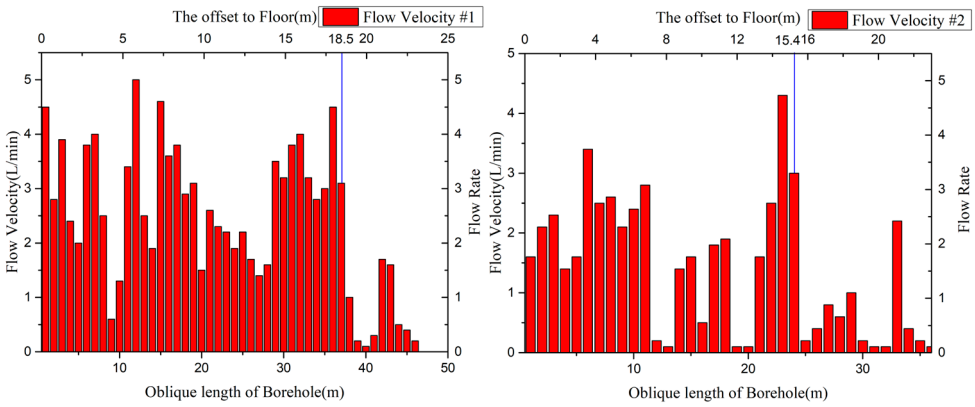


Figure 17. Curve of drilling leakage in the floor of the goaf.

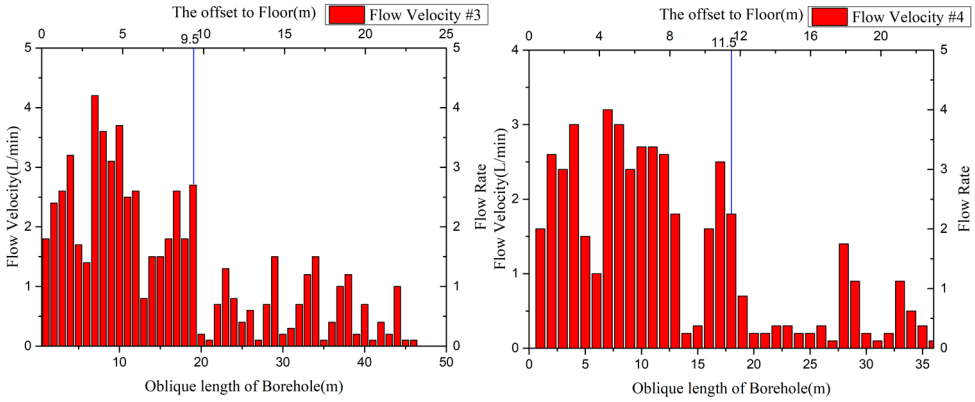


Figure 18. Curve of drilling leakage in the floor of the unmined area.

By observing the water leakage from six boreholes in the floor, the depth of the floor damage zone in the mining area has been determined. In the goaf, where the roof has collapsed completely and the floor has been re-compacted, the measured depth of the damage zone ranges from 15 m to 19 m. In the unmined area of the working face, the depth of floor damage is determined to be around 9 m to 12 m, indicating that the floor in the unmined area is less affected by mining. The floor damage in this area is related to the adjacent mined-out area. In the current mining area of the working face, the maximum depth of floor damage is between 19 m and 21 m. In this area, the floor is subjected to a strong load from the hard roof and experiences intense disturbances due to coal mining, resulting in severe floor damage. The maximum depth of damage is around 21 m. Considering that the thickness of the floor water-bearing layer is between 20 m and 32

m, with the minimum thickness being less than the maximum depth of floor damage, it is necessary to manage the roof and floor before mining to prevent the communication of water and ash from the floor, which can be harmful to mine production.

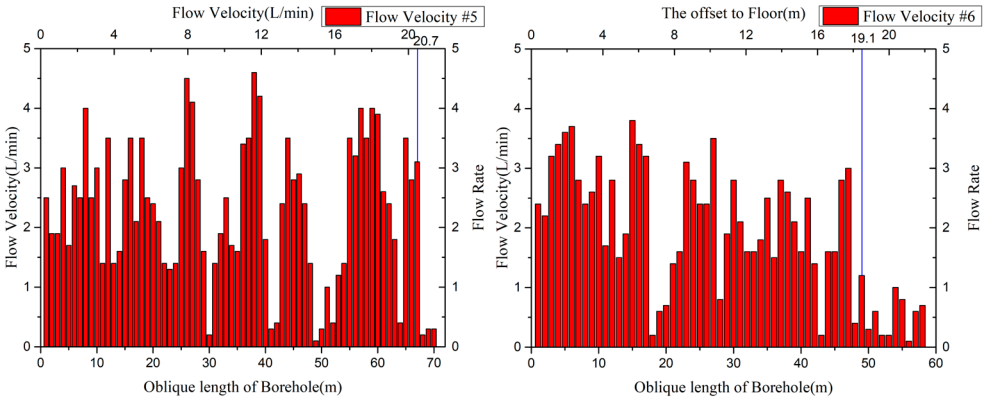


Figure 19. Curve of drilling leakage of the floor at coal wall of working face.

3.6. Chapter Summary

In this section, five different methods were used to calculate, predict, and measure the depth of floor damage. From Table 3, it can be observed that the maximum depth of floor damage measured using the double-end water-blocking device in the field is the largest. When compared with the measured values, the absolute error of the empirical formula calculation is 12.97 m, with a residual of 62.66%. This empirical formula is not suitable for calculating the depth of floor damage in a working face with a thick-hard roof. The maximum depth of floor damage calculated by the mathematical model analysis has an absolute error of 5.4 m, with a residual of 26.09%, providing some reference value but with a relatively low accuracy. Comparatively, the depth of floor damage predicted by the BP neural network deep learning model has an absolute error of 2.13 m, with a residual of 10.3%, which is closer to the actual values, with a smaller error and higher accuracy. It has a high practical value in the actual production process.

Table 3. Calculation and prediction of the measured floor failure depth value by different methods.

	Theoretical Model Calculation	BP Neural Network Calculation	Empirical Formula Calculation	In Situ Measurement
Maximum damage depth of the bottom plate	15.3	18.57	7.73	20.7
Relative error (measured value)	5.4	2.13	12.97	\
Residual error (measured value)	26.09%	10.3%	62.66%	\

4. The Temporal and Spatial Evolution Characteristics of Floor Damage during Mining of Coal Seams with Thick-Hard Roofs

Within the rock mass, there are many pre-existing fractures. When the rock layers are disturbed during mining, these micro-scale pre-existing fractures expand, connect, and penetrate to form macro-scale open fractures. Through in situ measurements of floor damage depth in coal seams with thick-hard roofs, it is observed that the high-stress zone in front of the coal wall has undergone fracture, and within the goaf, the floor inevitably exhibits bulging and uplift. The temporal and spatial evolution of floor rock mass strain along the working face reveals a continuous pattern of floor fracture zones, presenting a saddle-shaped morphology, as shown in Figure 20.

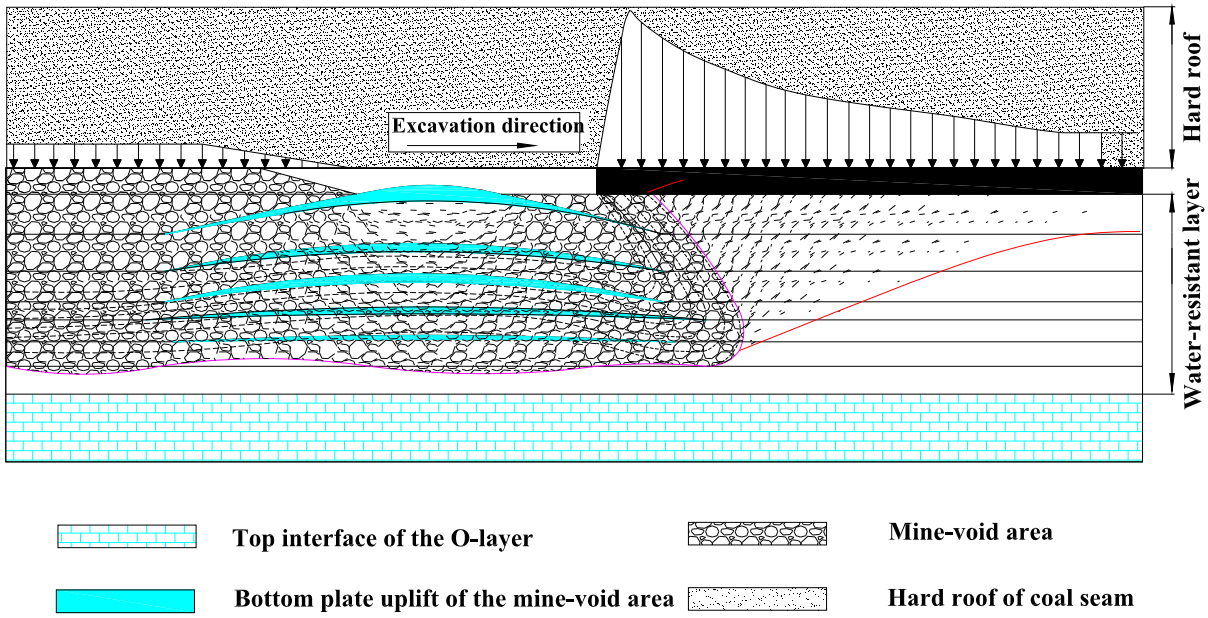


Figure 20. Distribution map of damaged area of coal seam floor in working face.

4.1. The Dynamic Temporal and Spatial Evolution Process of Floor Damage during Coal Seam Mining

During the process of coal seam mining, the floor undergoes three stages: compression, shear-sliding, and unloading. The shear-sliding and unloading stages are particularly prone to inducing floor damage and water inrush. As shown in Figure 21, in the presence of a thick-hard roof, the floor is subjected to high vertical stress, accompanied by intense disturbances caused by coal seam mining. In-field measurements have shown significant mining pressure on the working face. The floor rock mass near the coal wall experiences severe compressive shear deformation and slides towards the goaf. In the goaf, the floor rock mass is relieved of the high vertical stress, resulting in tensile failure due to the horizontal stress compression. This further increases the height of the floor damage zone and enhances the risk of floor water inrush. After mining, the goaf undergoes two stages: re-support and post-mining compaction. The re-support stage is prone to floor water inrush incidents, as the floor rock mass transitions from high stress to low stress state. The sudden release of stress can cause plastic deformation and failure in the coal seam floor, particularly when pre-existing and secondary fractures act together to form effective water-bearing channels. Pressurized water breakthrough can be extremely dangerous [47].

Based on the analysis of field measurements of advanced support pressure on a hard roof and in situ data of floor damage depth, the temporal and spatial evolution characteristics of floor deformation and failure under the conditions of mining coal seams with a thick-hard roof are revealed [14]. Prior to coal seam mining, the surrounding rock stress is in equilibrium. At a distance of 68.2 m before the coal seam is mined, the stress in the floor rock layer begins to significantly increase, and small cracks start to appear in the intact thin floor rock mass. As the working face advances, the high stress transmitted by the thick-hard roof combines with mining-induced disturbances, causing the floor rock layer to reach the strain value that leads to shear failure and forming the boundaries of a "saddle-shaped" pattern. After the working face passes, the vertical in situ stress of the overlying rock mass is relieved, and the interaction of two-dimensional stresses in the horizontal direction leads to tensile failure in the floor rock layer, resulting in floor heaving. The complete failure of the floor rock layer occurs, and as the roof of the goaf collapses and compacts, the floor rock layer experiences a decreasing trend in strain until it reaches a stable state.

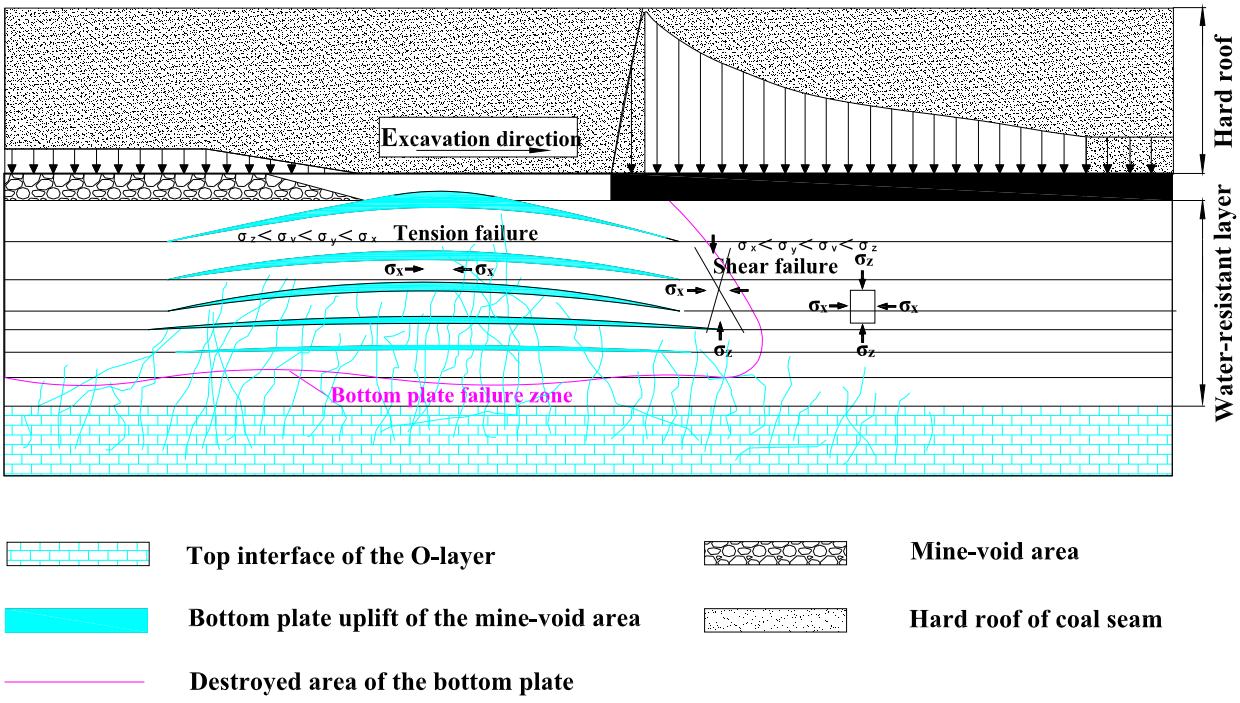


Figure 21. Spatial and temporal evolution map of coal seam floor in working face.

4.2. Dynamic Evolution Patterns of Floor Damage during Coal Seam Mining

During the coal seam mining process, the originally balanced stress in the surrounding rock is disrupted. As shown in Figure 22, the floor experiences a significant increase in concentrated stress from approximately 68.2 m before the extraction until it reaches a peak value approximately 6.5 m from the working face. This peak value is 1.8 times the original rock stress. The region of advanced stress concentration in the coal seam is significantly larger compared to mining conditions with a conventional roof. In the high-stress zone before mining, the floor rock mass begins to develop microcracks due to the influence of high vertical stress. As the coal seam working face advances, these microcracks gradually expand, forming secondary fractures and eventually forming a zone of stress release after extraction. Concurrently, with the collapse of the thick-hard roof, the goaf undergoes compaction to form a stress equilibrium zone after extraction.

One of the key issues in the formation of floor water inrush in coal seams is the formation of water channels. For intact floors without structural disruption, water inrush occurs mainly because the damaged zone in the floor establishes a connection with the water-conducting zone under pressure, forming a fractured water channel. For incomplete floors with structural disruptions, the main cause of water inrush is the connection between the activated structure and the water-conducting zone under pressure. Under the influence of strong loads in coal seams with thick-hard roofs covering the floor, and the disturbance caused by coal seam extraction, minor changes in the stress state of the floor can occur. These changes indirectly affect the depth of the floor damage zone and changes in the height of the water-conducting zone under pressure, and subsequently influence the evolution and formation of water channels in the floor. As shown in Figure 23, this section will describe the classic characteristics of water inrush patterns in thin floors under thick-hard roof conditions, serving as a reference for similar mining areas.

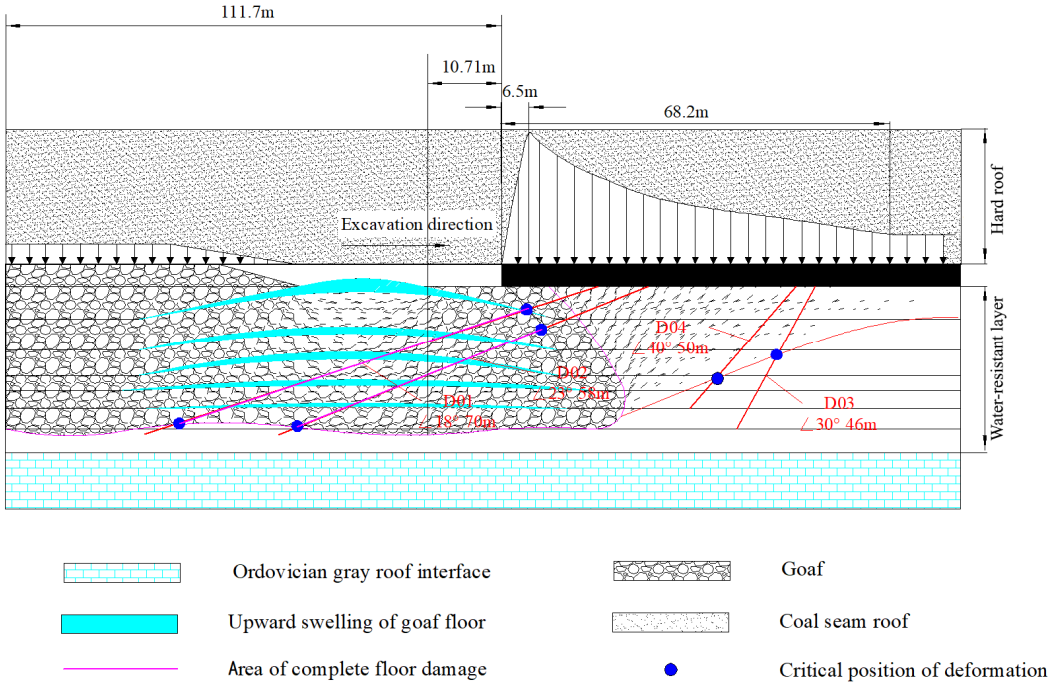


Figure 22. The evolution of the strain zone in the spatial and temporal dimensions along the strike of the coal face floor.

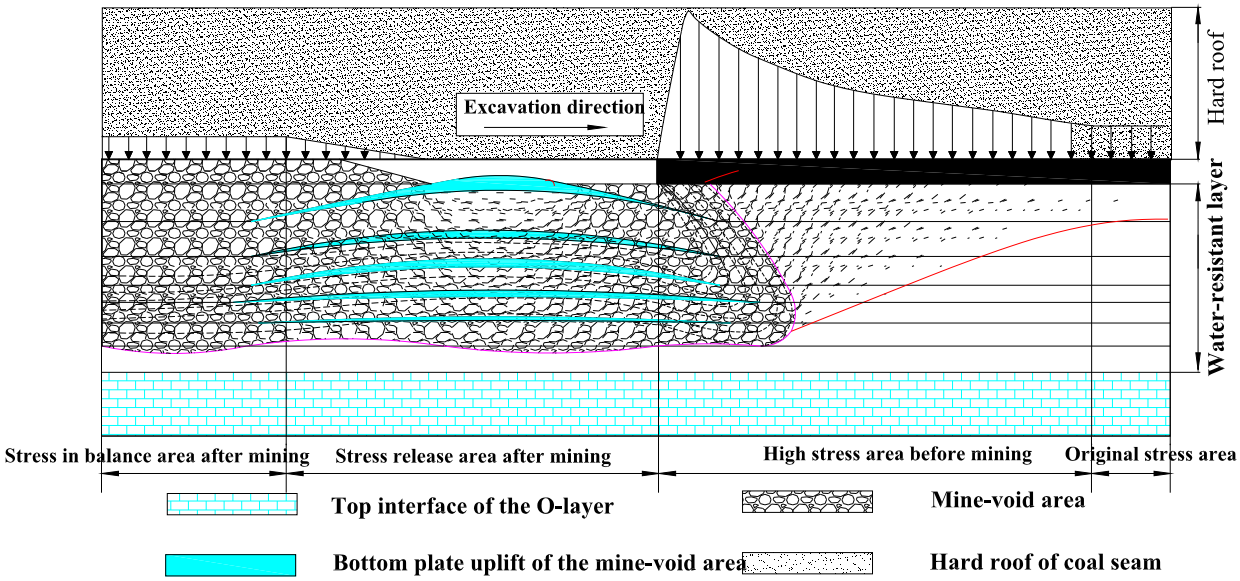


Figure 23. Partition diagram of the floor after mining of coal seam floor in working face.

4.3. The Communication Mode between the Floor Damage Zone and the Aquifer in Coal Mining

(1) Communication between high-stress-induced floor damage zone and aquifer upconing.

In the northern coalfield, the connection between the bottom floor of the coalfield and the overlying aquifer is closely related to the structural connections. However, in areas without structural connections, there is still a risk of aquifer water communication when the bottom floor's aquitard is thin. As shown in Figure 24, in the thin aquitard bottom floor, there may be one or more layers of thin limestone. Before mining, the stress of the surrounding rock and the water pressure is in a balanced state, and pressured water remains stationary after rising to a certain height in fractures. After mining, the vertically

downward high stress is relieved, causing the bottom floor to experience horizontal and upward vertical stress. The horizontal stress squeezes the bottom floor, causing fracture deformation. Under the influence of high stress from pressured water, the aquifer water slowly infiltrates, expands, and fractures along the secondary fractures formed by the rupture of the bottom floor. It gradually rises upwards. The thin limestone in the thin aquitard floor can serve as a transit station, providing a water source for the aquifer water until it communicates with the coal bed floor damage zone. The water breakout starts from a point, then expands along the channel, and eventually forms a line breakout, leading to large-scale scattered water flow.

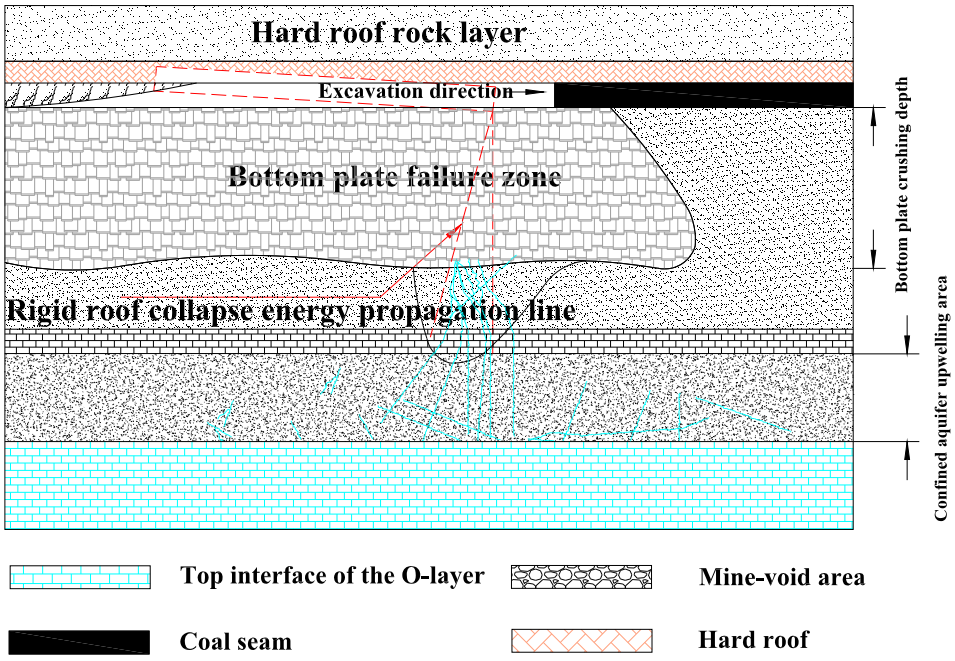


Figure 24. Schematic diagram of the conduction between the failure zone of the working face bottom plate and the austenitic ash guide zone.

(2) Communication between the bottom floor damage zone of the coal seam and water-conducting structures

In the context of coal mining under thick-hard roof strata conditions, the communication between the bottom floor damage zone and water-conducting structures is the most common mode of bottom floor water inrush. In the majority of underground mines with high-pressure mining, there is a risk of bottom floor damage zone connecting with water-conducting structures, leading to water inrush. These water-conducting structures mainly include activated water-conducting columns and water-conducting faults. In the history of coal mining in the northern coalfields, these water-conducting structures have caused significant water inrush accidents, resulting in substantial economic losses. In this section, a brief analysis will be provided for these two water inrush modes, aiming to provide a reference for the prevention and control of bottom floor water inrush in coal seams under thick-hard roof strata conditions.

Before coal mining, faults, despite undergoing long-term geological activity, remain in a state of stress equilibrium. However, with the initiation of coal seam mining, this natural balance is disrupted, and the stress state changes. The fault may experience movement. As shown in Figure 25, if a pressurized water-bearing fault intersects the coal seam bottom floor, relative movement along the fault plane can easily establish communication between the bottom floor damage zone and the upward water-conducting zone, leading to bottom floor water inrush accidents. Generally speaking, reverse faults have stronger structural stability compared to normal faults, resulting in a relatively lower probability of water inrush. The

location and distance between the fault and the mining face also affect the stability of the fault. Therefore, before mining under pressurized water conditions, necessary measures should be taken to investigate the distribution of faults. Precautions such as using water-resistant coal pillars, drainage, and pressure reduction techniques, or grouting to reinforce faults, should be implemented to ensure the safe production of the mining face.

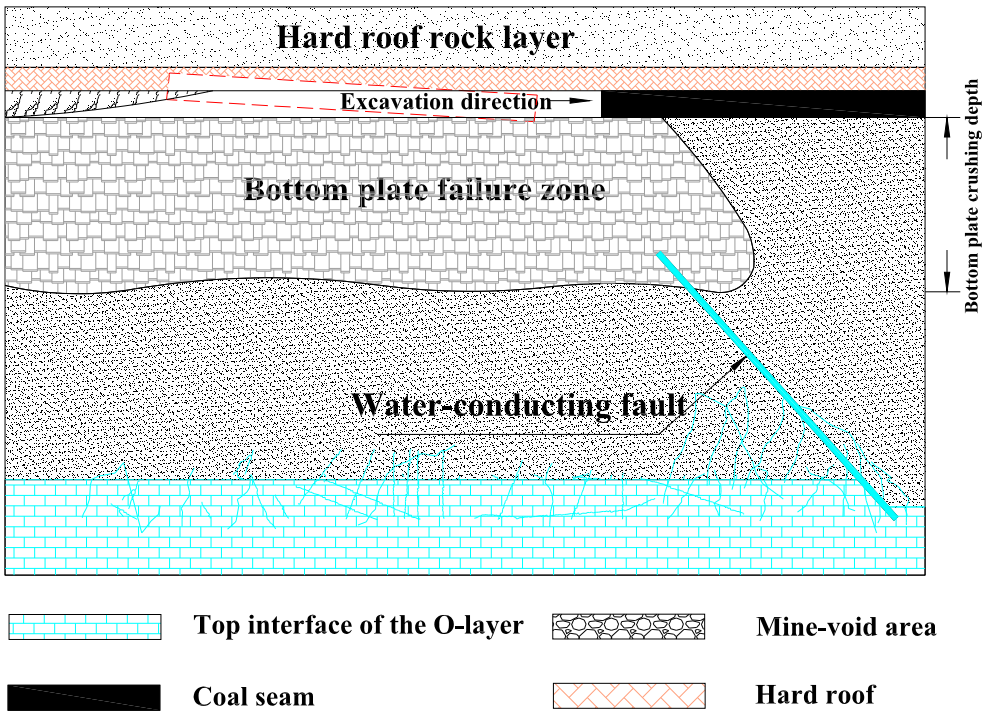


Figure 25. Schematic diagram of the conduction between the floor failure zone and the water-conducting fault.

Collapse columns can take on various forms, with irregular circular, elliptical, or irregular polygonal cross-sectional shapes, and can be broadly classified as cylindrical or conical based on their three-dimensional shape. The occurrence of bottom floor water inrush induced by collapse column structures primarily depends on the relationship between the collapse columns and the mining face or roadway. It can be divided into two main modes: the top-bottom water inrush mode and the sidewall water inrush mode. In the top-bottom water inrush mode, when there is no intersection between the mining face or roadway and the collapse columns, the water inrush point is mainly located at the top or bottom of the collapse columns. On the other hand, in the sidewall water inrush mode, the collapse column intersects with the mining face or roadway, leading to bottom floor water inrush, and the water inrush point is typically found along the sidewall of the collapse column, as shown in Figure 26. Karst collapse columns are formed by the collapse of overlying rock layers on karst cavities. Under the continuous influence of groundwater erosion, they take on cylindrical or irregular shapes. The internal structure of the collapse columns is altered by long geological processes, creating sufficient space that serves as the necessary conditions for both water-conducting channels and water pressure for water inrush.

Several basic conditions must be met for the communication and water conductance between collapse columns and the coal seam's damaged zone: (1) Karst collapse columns must be connected to the highly permeable aquifers of the Middle-Upper Ordovician system. Without water connectivity, there can be no water conductance. (2) The karst groundwater in the region where the collapse columns are located should have sufficient pressure to overcome the resistance of the compacted rock fragments within the column and effectively infiltrate upward. (3) The collapse columns themselves should have strong water-conducting properties, which are determined by the degree of compaction and cementation

of the infill material. A better-cemented infill material with a lower porosity will have weaker water-conducting properties, while a less-cemented infill material will have stronger water-conducting properties. Exploration of collapsed columns can be challenging, and physical exploration methods are commonly used. However, in the northern coalfields, the distribution of cemented materials within the collapsed columns is uneven. Therefore, drilling is required to analyze and confirm suspected collapse column structures, and grouting is used to seal and reinforce the confirmed collapse column structures.

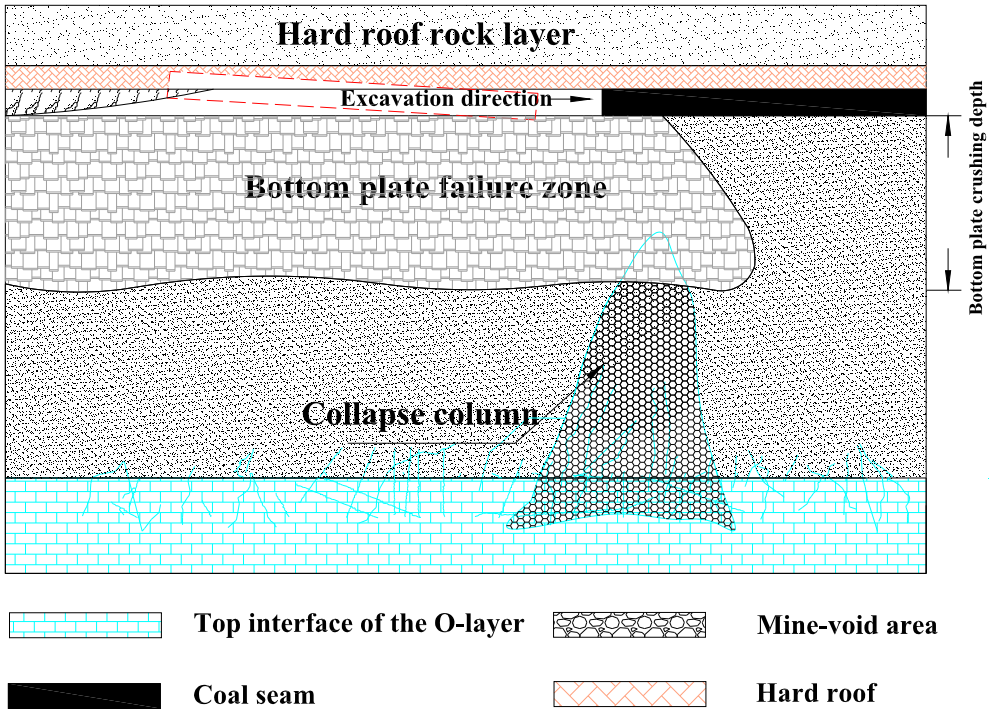


Figure 26. Schematic diagram of the conduction between the floor failure zone and the water-conducting collapse column.

5. Discussion

Based on the case study of the Guo'er Zhuang coal mine, where thick-hard roof strata with a thin bottom floor are subjected to high-pressure mining, this study investigated the mechanism of water inrush from the thick-hard roof aquifer layer in the context of mining-induced bottom floor deformation. The study established the mechanism of bottom floor damage and the mode of fracture water inrush in the context of high-pressure mining with a thin bottom floor.

Based on the theory of plastic mechanics, the study solved for the depth of bottom floor failure and the range of bottom floor failure within the goaf. The study employed double-end water stoppers to observe the depth of bottom floor failure in the unmined area of the working face, the vicinity of the working face, and the adjacent goaf. The maximum observed depth of bottom floor failure was determined to be 21 m. A three-dimensional numerical model was established using FLAC3D5.0 numerical simulation software. This model provided the distribution of stress, strain, and plastic zone during bottom floor failure. This study reveals that the maximum vertical stress on the working face is 40 MPa, and that the mining-induced stress stabilizes after the face advances to 80 m. The maximum displacement of the roof strata is 18 cm, and there is not much change in displacement during the excavation process. Additionally, the study establishes mechanical models for different working conditions: normal sandstone roof conditions, thick-hard roof conditions, and thick-hard roof conditions with confined water pressure. FLAC3D simulation is performed for these conditions, and it is observed that under thick-hard roof conditions, stress concentration and its influence range are significantly higher than

under conventional conditions. High-strength loads on the thick-hard roof are found to be the key influencing factors for floor rock mass damage. By comparing and analyzing the calculated area of bottom floor failure based on plastic mechanics theory, the morphology of bottom floor failure after high-pressure mining with a thick-hard roof strata and a thin aquitard layer was determined. This analysis led to an understanding of the bottom floor failure mechanism and water inrush mechanisms under these conditions. A deep learning model for predicting the depth of coal seam bottom floor failure was established using the BP neural network learning method. The model was trained with data from 100 different mine working faces, including factors such as depth of mining, coal seam dip angle, mining thickness, the oblique length of the working face, and whether there were structural intersections. The model was applied to predict the depth of bottom floor failure for working face 29205 in the Guo'er Zhuang coal mine. The relative error between the predicted value and the true value was 2.13%, the residual was 10.3%, and 93.3% of the sample residuals were distributed within ± 4. These indicators confirmed the accuracy of the BP neural network for predicting the depth of bottom floor failure and provided a useful approach and algorithm for predicting the depth of bottom floor failure under similar mine conditions.

6. Conclusions

Based on various methods such as theoretical calculations, numerical simulations, empirical formulas, on-site measurements, and floor failure prediction models, the depth and range of floor failure have been analyzed, and the following conclusions have been drawn:

1. At a depth of 68.2 m before mining, the stress in the bottom floor rock layer begins to increase significantly, and small cracks start to appear in the intact thin aquitard layer. Along with the mining-induced disturbances, the high stress transferred from the thick-hard roof strata causes the bottom floor rock layer to reach the shear failure strain, forming a "saddle-shaped" boundary. In the goaf area, the vertical stress of the overlying strata is relieved, leading to the interaction of horizontal stresses that result in the stretching and failure of the bottom floor, creating a bottom heave. The bottom floor rock layer is completely damaged, and with the collapse and compaction of the goaf roof, the strain in the bottom floor rock layer gradually decreases and reaches a stable state.
2. The main modes of floor water inrush under thick-hard roof conditions include the high-stress-induced connection between bottom floor damage zones and water-bearing layers; the connection between mining-induced damage zones and water-conducting faults; the connection between mining-induced damage zones and water-conducting collapse columns; and the water inrush coupling mode between mining-induced damage zones and high-pressure water floors.
3. In the pre-mining high-stress zone, the floor first undergoes shear failure, followed by stretching failure as the high stress gradually releases. In the post-mining stress relief zone, the floor rock mass mainly experiences stretching failure, causing the floor to heave after stretching failure occurs in each rock layer. As the goaf roof collapses and compacts, the floor is again compacted, and the bottom floor stress eventually reaches an equilibrium state.

Author Contributions: Conceptualization, M.C. and S.Y.; Software, S.L.; Formal analysis, X.W.; Writing—original draft, M.C.; Writing—review & editing, S.Y. All authors have read and agreed to the published version of the manuscript.

Funding: National Natural Science Foundation of China Youth Fund (42202291).

Data Availability Statement: Data available in a publicly accessible repository.

Conflicts of Interest: The authors declare no conflicts of interest.

References

1. Mu, W.; Li, L.; Zhang, Y.; Yu, G.; Ren, B. Failure mechanism of grouted floor with confined aquifer based on mining-induced data. *Rock Mech. Rock Eng.* **2023**, *56*, 2897–2922. [CrossRef]
2. Zhang, J.; Liu, T. On the depth and distribution characteristics of the coal floor mining-induced fracture zone. *J. Coal Sci.* **1990**, *15*, 46–55.
3. Zhang, J.; Liu, T.; Zhang, Y. Study on the permeability characteristics of fractured rock masses. *J. Coal Ind.* **1997**, *5*, 35–39.
4. Zhang, J.; Liu, T. Theory and practice of coal floor water inrush prediction. *Coal Geol. Explor.* **1989**, *4*, 38–41+71.
5. Qian, M.; Miao, X.; Xu, J.; Mao, X. *Key Layer Theory of Rock Stratum Control, Xuzhou*; China University of Mining and Technology Press: Xuzhou, China, 2003.
6. Qian, M.; Miao, X. Theoretical study on the rupture law of mining floor rock stratum. *Chin. J. Rock Mech. Eng.* **1995**.
7. Qian, M.; Xu, J.; Miao, X. Green mining technology in coal mines. *J. China Univ. Min. Technol.* **2003**, 5–10.
8. Wu, Q.; Wang, J.-H.; Liu, D.-H.; Cui, F.-P.; Liu, S.-Q. A new practical methodology of the coal floor water bursting IV: The application of AHP vulnerable index method based on GIS. *J. Coal Sci.* **2007**, *32*, 6.
9. Sun, W.; Zhou, W.; Jiao, J. Hydrogeological classification and water inrush accidents in China's coal mines. *Mine Water Environ.* **2016**, *35*, 214–220. [CrossRef]
10. Shi, L.; Qiu, M.; Wang, Y.; Qu, X.; Liu, T. Evaluation of water inrush from underlying aquifers by using a modified water-inrush coefficient model and water-inrush index model: A case study in Feicheng coalfield, China. *Hydrogeol. J.* **2019**, *27*, 2105–2119. [CrossRef]
11. Shangxian, Y.; Qiang, W.; Shangxu, W. Generalized multiple porous media seepage model of groundwater system for Fangezhuang Mine. *Chin. J. Rock Mech. Eng.* **2004**, *23*, 2319–2325.
12. Yin, S.; Wu, Q. Generalized modes and academic criterions of water inrush from paleo-sinkholes. *Chin. J. Eng.* **2006**, *28*, 812–817.
13. Yin, S.-X.; Wang, S. A numerical simulation analysis of influence of karstic collapse columns on rock mass yield and water inrush from coal floor. *Mei T'Hsueh Pao J. China Coal Soc.* **2003**, *28*.
14. Shi, X.Z. Study on the Damage Evolution and Water Damage Prevention of the Coal Mining Floor above the Deep and High Pressure Water. Ph.D. Thesis, China University of Mining and Technology, Xuzhou, China, 2020.
15. Yu, X.; Han, J.; Shi, L.; Wei, J.; Zhu, L.; Li, S. Forecast of destroyed floor depth based on BP neural networks. *J. China Coal Soc.* **2009**, *34*, 731–736.
16. Yang, J.X.; Lv, M.; Hao, C.X. Leakage failure form and leakage prediction of water supply network based on neural network deep learning and structure optimization. *Hydroelectr. Energy Sci.* **2020**, *38*, 87–90.
17. Wolkersdorfer, C.; Bowell, R. Contemporary reviews of mine water studies in Europe, part 1. *Mine Water Environ.* **2004**, *23*, 162–182. [CrossRef]
18. Ma, J.; Zhan, B.; Luo, C. Analysis of floor failure and water inrush risk assessment of Luoling mine II 1018 working face. *J. Chin. Foreign Entrep.* **2014**, 151+153.
19. Zhang, W.; Zhao, K.; Zhang, G.; Dong, Y. Prediction of floor failure depth based on grey correlation analysis theory. *J. China Coal Soc.* **2015**, *40*, 53–59.
20. Guo, Z.A.; Yang, X.; Yang, J.F.; Jiang, H.B.; Zhang, H. Failure depth prediction method of stope floor based on PCA-BP neural network model. *China Sci. Technol. Pap.* **2021**, *16*, 468–474.
21. Cui, K.; Jing, X. Research on prediction model of geotechnical parameters based on BP neural network. *Neural Comput. Appl.* **2019**, *31*, 8205–8215. [CrossRef]
22. Xue, X.C.; Tina, F.F. Coal floor failure depth Prediction based on data optimized BP neural network. *Chin. Coal Geol.* **2021**, *33*, 8–12.
23. Xu, Y.Z. A study on the depth of floor damage in lower coal seam with water pressure in Gequan coal mine. *China Coal* **2010**, *36*, 48–51.
24. Lu, Y. Depth determination of floor failure zone in 14,311 fully mechanized caving face. *Coal Chem. Ind.* **2017**, *40*, 52–54.
25. Yu, J.J. Observation on three-zone development height of roof and floor in large-mining-height working face with medium-hard overburden rocks. *Shanxi Meitan* **2013**, *33*, 34–35+41.
26. Zhao, Y.P.; Qiu, M.; Liu, X.F.; Shi, L.Q. GRA-FOA-SVR model for prediction of failure depth of coal seam floor. *China Sci. Pap.* **2018**, *13*, 247–252.
27. Zhang, F.D. Multi-factor nonlinear prediction model of floor damage depth in deep. *Coal Min.* **2018**, *23*, 92–95.
28. Yang, G.; Yin, S.; Ren, R.; Kang, X.; Liu, D.; Zhang, B.; Li, W.; Xie, Y.; Hao, C.; Li, J.; et al. Research on the Distribution Law of the Upper Three Zones of the Main Coal Seam and the "Lower Three Zones" of the Mine under Pressure Mining in Xishan Mine. Shanxi Province, Xishan Coal and Electricity, 27 December 2018. Available online: https://kns.cnki.net/kcms2/article/abstract?v=sxrP1m9hSI-F8i1-qHBlFl5SxxUe3SHsT_FeZ6ibUefHTYtO7ljJCCEs4mOmicO5hCiK0OWZSF709vDZNg4hHL0b1Adxf-Bxiks6dD5N6aROrSlZ_pXJ8huHHSYkPCVom8oxApwOPwZiRi4StLl5XJx28s3W_iGrTYTYn4QRPQ6uGw-qUcpStF8ifPggIogY&uniplatform=NZKPT&language=CHS (accessed on 6 August 2024).
29. Yu, X.G.; Han, J.; Wang, D.D.; Cong, P.Z.; Ji, L.J. Floor damage depth prediction based on theory of fuzzy comprehensive evaluation decision. *Coal Technol.* **2016**, *35*, 158–160.
30. Sun, Z.Y.; Meng, X.Z.; Hao, D.Y.; Dong, S.Y.; Liu, A.Q. Study on influence of the length of working face on failure depth of floor in mining above aquifer. *Min. Res. Dev.* **2020**, *40*, 22–27.

31. Yang, C. Application of network parallel electrical method in depth detection of thick coal seam floor damage. *Inn. Mong. Coal Econ.* **2020**, *15*, 146–148.
32. YW, C. Detection and analysis of floor failure depth in coal mining face. *Shaanxi Coal* **2018**, *37*, 24–26+42.
33. Su, P.L.; Gu, S.C.; Li, A. Analysis on site measurement and simulation of floor failure depth under condition of deep mining depth in Dongjiahe mine. *Coal Eng.* **2014**, *46*, 93–95.
34. Fei, L.; Jinling, Z.; Lihong, D. Numerical simulation study on evolution of mining dynamic fracture for seam floor. *Coal Sci. Technol.* **2014**, *42*, 37–39.
35. Li, A.; Gu, S.; Chen, F. Theoretical Analysis and Numerical Simulation of Destroyed Depth of Coal Seam Floor During Bearing Mining: With Seam No. 5 in Dongjiahe Mine, Chenghe Mining Area, Shaanxi as Example. *Coal Geol. Explor.* **2013**, *41*, 56–60.
36. Han, L.; Meng, X.R.; Wang, J. Analysis as well as monitoring and measure on floor failure depth of No. 663 coal mining face of Liuqiao No.1 mine. *Coal Eng.* **2013**, *45*, 74–77.
37. Chen, C.L.; Yao, D.X.; Zhao, K.; Yang, Q.; Cheng, G. Floor 10 damage depth of green east coal mine based on grey neural network. *Coal Technol.* **2012**, *31*, 49–51.
38. He, T.; Li, G.-D.; Sun, C.; Luo, F.; Li, X.-Q. Floor failure characteristics of thick coal seam mining above confined aquifer. *Min. Metall. Explor.* **2022**, *39*, 1553–1562. [CrossRef]
39. Zhang, S.W. Analysis of key layers of water-resistance of coal roof and floor and evaluation of its destruction ability. *China Energy Environ. Prot.* **2020**, *42*, 34–37+42.
40. Zhao, Y.; Nan, J.; Cui, F.-Y.; Guo, L. Water quality forecast through application of BP neural network at Yuqiao reservoir. *J. Zhejiang Univ.-Sci. A* **2007**, 1482–1487. [CrossRef]
41. Trebar, M. Use of MATLAB Neural Networks Toolbox in a character recognition problem. *Comput. Appl. Eng. Educ.* **2005**, *13*, 66–71. [CrossRef]
42. Zhu, H.; Lu, X. The prediction of PM2.5 value based on ARMA and improved BP neural network model. In Proceedings of the 2016 International Conference on Intelligent Networking and Collaborative Systems (INCoS), Ostrava, Czech Republic, 7–9 September 2016; IEEE: New York, NY, USA, 2016.
43. Kalkan, E.; Reyes, J.C. Significance of rotating ground motions on behavior of symmetric-and asymmetric-plan structures: Part II. Multi-story structures. *Earthq. Spectra* **2015**, *31*, 1613–1628. [CrossRef]
44. Wang, G.; Li, P.; Wu, Q.; Cui, X.; Tan, Z. Numerical Simulation of Mining-Induced Damage in Adjacent Tunnels Based on FLAC3D. *Adv. Civ. Eng.* **2021**, *2021*, 9855067. [CrossRef]
45. Murphy, M.M.; Ellenberger, J.L.; Esterhuizen, G.S.; Miller, T. Analysis of roof and pillar failure associated with weak floor at a limestone mine. *Int. J. Min. Sci. Technol.* **2016**, *26*, 471–476. [CrossRef] [PubMed]
46. Cao, M.; Yin, S.; Xu, B. Water inrush and failure characteristics of coal seam floor over a confined aquifer. *Energy Rep.* **2021**, 8298–8311. [CrossRef]
47. Fontara, I.-K.M.; Kostinakis, K.G.; Manoukas, G.E.; Athanatopoulou, A.M. Parameters affecting the seismic response of buildings under bi-directional excitation. *Struct. Eng. Mech.* **2015**, *53*, 957–979. [CrossRef]

Disclaimer/Publisher's Note: The statements, opinions and data contained in all publications are solely those of the individual author(s) and contributor(s) and not of MDPI and/or the editor(s). MDPI and/or the editor(s) disclaim responsibility for any injury to people or property resulting from any ideas, methods, instructions or products referred to in the content.